UCRL-53750
Distribution Category UC-21

MASTER

Preparation and Properties of Polyvinyl Alcohol Microspheres

UCRL--53750

DE86 015111

J. H. Campbell, J. Z. Grens, J. F. Poco,

and B. H. Ives

Manuscript date: June 1986

LAWRENCE LIVERMORE NATIONAL LABORATORY
University of California • Livermore, California • 94550

Available from: National Technical Information Service • U.S. Department of Commerce
5285 Port Royal Road • Springfield, VA 22161 • A02 • (Microfiche A01)

Contents

SYMBOLS

Symbol	Definition	Units
ΔH	Latent heat of the evaporating solvent	J/g
ΔP	Pressure difference	atm
$\Delta\rho$	Density difference	g/cm^3
ΔT	Difference between gas and droplet temperature	K
λ	Heat of vaporization	J/g·mol
$\lambda_{i,}$	Heat of vaporization for i^{th} component	J/g·mol
μ	Viscosity	g/cm·s (poise)
ν	Poisson's ratio	—
ρ	Density	g/cm^3
$\rho_{D,}$	DT density	g/cm^3
ρ_g	Gas density	g/cm^3
ρ_p	Polymer density	g/cm^3
ρ_s	Solution density	g/cm^3
σ_c	Compressive strength	psi
A	Area	cm^2
A_k	Coefficient describing permeability	mol(STP)/cm·cm^2·s·atm
A_p	Projected particle area	cm^2
A_s	Scan area	cm^2
B	Permeability temperature coefficient	K
C_d	Drag coefficient	—
C_f	Molar concentration	mol/l
C_p	Heat capacity	J/mol·K
D	Diameter	cm
D_0	Initial drop diameter	cm
D_R	Radiation dose	rad
D_f	Drop diameter at film formation	cm
D_i	Diffusion coefficient of i^{th} component	cm^2/s
D_p	Drop particle diameter	cm^2
E	Young's modulus	psi
E_d	Average beta energy	keV
E_D	Energy deposition	keV/g
E_e	Energy of electron beam	erg
F	Force	Dyne
F_b	Force of buoyancy	Dyne
F_d	Force of drag	Dyne
F_g	Force of gravity	Dyne
K_p	Permeability	mol(STP)/cm·cm^2·s·atm
K_{xm}	Mass-transfer coefficient	g·mol/cm^2·s·atm
M_{DT}	Molecular weight of DT	g/mol
N_A	Avogadro's number	—
N_T	Number of tritium atoms in source volume	—
P	Pressure	atm
P_b	Buckling pressure	psi
P_c	Pressure at compressive failure	psi
$\dot{Q}$	Rate of heat transport	J/s
R	Universal gas constant	cm^3·atm/mol·K
R_b	Range of beta emission	g/cm^2
T	Temperature	K
T_a	Average temperature across boundary layer	K
T_g	Column purge gas temperature	K
T_s	Adiabatic saturation temperature	K

U	Velocity	cm/s
U_t	Terminal velocity	cm/s
V	Volume	cm^3
X	Mole fraction of i^{th} component	—
X_{DT}	Penetration depth in DT	cm
X_p	Penetration depth	cm
a	Factor for transpiration correction	—
f_c	Correction factor	—
g	Gravitational constant	980 cm/s^2
h	Convective heat-transfer coefficient	$J/cm^2 \cdot s \cdot K$
i_0	Electron beam current	e^-/s
k_f	Thermal conductivity	$J/cm \cdot s \cdot K$
k_g	Gas thermal conductivity	$J/cm \cdot s \cdot K$
m	Mass	g
$\dot{m}$	Mass rate	g/s
$\dot{m}_{max}$	Maximum fill rate	g/s
m_p	Mass of polymer exposed	g
r_s	Shell radius	cm
t	Time	s
$t_{1/2}$	Tritium half-life	y
t_d	Drop drying time	s
t_w	Wall thickness	cm

Dimensionless Numbers

Re	Reynolds number
Pr	Prandtl number
Sc	Schmidt number
Nu	Nusselt number

Preparation and Properties of Polyvinyl Alcohol Microspheres

Abstract

Polyvinyl alcohol (PVA) microspheres, having a size range of ~150- to 250-μm diameter with 1- to 5-μm wall thickness, have been fabricated using a solution droplet technique. The spheres were developed for possible use on the Lawrence Livermore National Laboratory (LLNL) Inertial Confinement Fusion (ICF) Program.

PVA, a polymer chosen based on earlier survey work carried out at KMS Fusion, Inc., has good strength, low hydrogen permeability, is optically transparent, and water soluble. The latter property makes it safe and easy to use in our droplet generator system.

A unique dual-orifice droplet generator was used to prepare the spheres. The droplet generator operating conditions and the column processing parameters were chosen using results from our 1-D model calculations as a guide. The polymer microsphere model is an extension of the model we developed to support the glass sphere production.

After preparation, the spheres were physically characterized for surface quality, sphericity, wall thickness (and uniformity), and size. We also determined the buckling pressure for both uncoated and CH-coated spheres. Radiation stability to beta decay (from tritium) was evaluated by exposing the spheres to a 7-keV electron beam. The results from these and other physical property measurements are presented in this report.

Introduction

The basic target used in many laser fusion experiments is a hollow microsphere. Generally, these microspheres have been made from silicate glasses,[1,2] however, recent target-design work emphasizes the need for a lower-density, lower-atomic-number material. To meet this need, we have recently prepared target-quality microspheres from polyvinyl alcohol. This report summarizes the experimental and modeling studies done at LLNL in support of this work.

At first glance, there appears to be several materials that could be used to prepare low-Z/low-density microspheres: e.g., beryllium, lithium, lithium hydrides, boron hydrides, lithium borate glasses, and organic polymers. However, apart from having low density and low atomic number, the sphere material must also meet a number of other specifications; the most critical of these are listed in Table 1. Through a process of elimination, we found that organic polymers are presently the best-suited materials for meeting these specifications.

Research on fabrication of polymer microspheres has been ongoing for some time in the laser fusion community. In this country, the first efforts were by Kool et al. at KMS Fusion Inc. (KMSF).[3] They examined a number of polymers and attempted fabrication by both droplet drying and micro-encapsulation techniques. Their early efforts showed that PVA was one of the best candidates for a shell material. This choice was based primarily on PVA's excellent gas retention properties and high tensile strength. Also, PVA is water soluble; we can thus avoid the problem of dealing with toxic solvents.

Recently, Shiraga et al.[4] in Japan have reported use of polyethylene microspheres in studies of ablation-pressure distribution. The microspheres were 140 μm in diameter with a wall thickness of 4 to 5 μm and had a 2-μm-thick coating of beryllium. Details of the fabrication technique were not reported.

Polymer microsphere work in Britain[5] and Russia[6] has focused on polystyrene although the

Table 1. Desired microsphere material properties.

- Good gas retention (for DT) at 25°C.
- High tensile/compressive strength and high Young's modulus.
- Optically transparent.
- High melting/decomposition temperature.
- Corrosion and abrasion resistant.
- Low density (<1.0 g/cm^3).
- Low Z (<3 to 4).
- Good film-forming characteristics.
- Radiation stability.

fabrication techniques differed. The British have used a micro-encapsulation technique, and they report preparation of spheres ~50 to 500 μm in diameter. The Russian work, on the other hand, has relied mainly on the use of polystyrene particles impregnated with a hydrocarbon blowing agent. They report preparation of spheres varying in size from 70 to 1600 μm by the addition of 2 to 7 wt% pentane. The impregnated polystyrene was then dropped through a heated column held at a reduced pressure.

For use in an ICF target, the microsphere material preferably has good gas retention properties at room temperature coupled with high tensile strength. Also, since a droplet method is used to prepare the spheres, the polymer must be a good film former.

A survey of common polymers gave several potential candidates. From these, polyacrylonitrile, polyvinyl alcohol, and sodium carboxymethyl cellulose were chosen for initial study. (Note that polystyrene was not chosen because of its poor gas retention at room temperature.) Based on these initial experiments, we ultimately selected PVA as the best polymer for the Novette application. We chose PVA for several reasons. First, its strength and gas retention properties (particularly for hydrogen) were the best. Second, PVA is readily available and well characterized. Thus, a data base of physical and chemical properties was available and a constant supply of a suitable feed stock could be relied on. Third, the drying and film forming properties of PVA solutions were well suited for our droplet method of microsphere formation. Fourth and finally, we could build on the initial work done at KMS Fusion Inc. on preparing PVA spheres.

This report is divided into three main sections. In the first section, we discuss the droplet method used to prepare the microspheres; we also present details of the properties and composition of the starting solution, the experimental set-up (drying column and droplet generator), and the effects of various process parameters. In the second section, we describe the mathematical model that was developed to help quantify our understanding of the microsphere formation process. The third section summarizes the results of property tests and measurements that were carried out on the final microspheres.

Target Quality Specifications

At LLNL, the current specifications on microspheres used in ICF experiments are very stringent. Acceptable shells must fall within a diameter tolerance of ± 5 μm of the specified design size. Furthermore, the average wall thickness of the shell must be within ± 0.5 μm of the design value with a uniformity of ± 0.1 μm. Defects on the surface finish of the shells must be less than ~1000 Å.

The conformance of the spheres to these specifications is continuously checked by an extensive battery of quality assurance tests. Those coated spheres that are selected for ICF experiments are subjected to 4π examination to verify all critical target dimensions and map any small surface defects.

We prepared PVA spheres with diameters in the range of 150 to 250 μm and wall thicknesses of about 1 to 5 μm. The wall thickness could be increased by application of a CH coating using a RF plasma polymerization technique.[7]

Microsphere Production System

The PVA microspheres were prepared using a dual-orifice droplet generator and a heated drying column as schematically shown in Fig. 1. In brief, the process involves the formation of uniform

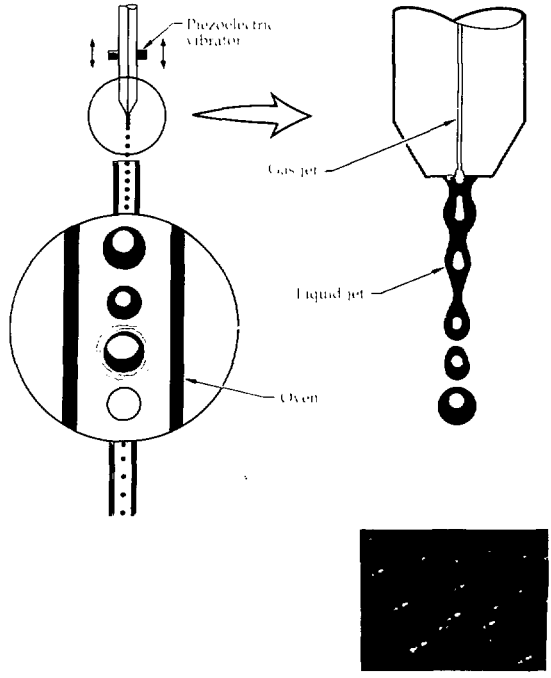

Figure 1. Schematic diagram of the droplet technique used to prepare PVA microspheres. The method differs from our previous work on glass microspheres in that a dual-orifice generator is used to produce uniformly-sized, hollow droplets. These droplets subsequently dry and expand into the final hollow spheres as they fall through a heated column. The inset shows an example of the final PVA sphere product.

hollow droplets of an aqueous PVA solution by acoustically breaking up a capillary jet of this solution. The droplets subsequently dry and blow to form the desired microsphere product (Fig. 1). The liquid droplet technique has major advantages:

- Excellent control of shell diameter and wall thickness,
- High production rate,
- Good surface quality.

In the text that follows, this method of microsphere fabrication is described in detail.

Preparation and Properties of the Polymer Solution

A solution of PVA in a 50/50 vol% mixture of methanol and water was used as a feedstock for our droplet experiments. The initial solution typically had a PVA (115 000 mol wt) concentration of only 1 wt%. This limitation was not based on solubility but rather on the viscosity of the solution that could be through the generator. In experiments where the lower-molecular-weight

PVA (85 000) was used, solutions of up to 2 wt% percent could be successfully run through the generator.

The combination of usable solvents and of approximate solution concentrations were recommended to us by Crawley[8] based on early work by Kool et al. at KMSF.[3] The procedure used to prepare the starting compositions was also adopted from Crawley[8] although some minor changes were made to accommodate our particular generator. KMSF found that a 50/50 methanol and water feedstock gave the best results in their spray dryer method of sphere preparation. For our system, the product quality is insensitive to the exact amount of methanol as long as it is in the range of 30 to 50%. Solvent mixtures outside this range generally gave poorer quality spheres.

The starting solutions were prepared by slowly adding 1-wt% PVA (ground to less than ~1-mm particles) to 80°C distilled water in a flask. The flask was heated using a standard heating mantle. The water was continuously stirred during the addition and after. Generally, PVA goes into solution within about one to two hours.

At this point, the PVA solution is quite stable and can be stored at room temperature for several days prior to addition of methanol. However, we found that once the methanol is added, the solution must be used within a few hours. Beyond this time, some gel formation occurs and the solution cannot be run through the generator.

Before adding the methanol, the PVA/water solution is first cooled to about 60°C, then stirred continuously while the methanol is slowly dripped into the flask. A slight heating maintains the 60°C temperature. A reflux condenser connected to the flask controls methanol vapor evolution.

We did not make measurements of the solution viscosity but used values that have been reported in the literature for PVA/water systems.[9] These data are shown in Fig. 2. The solution viscosity is critical for proper droplet generator operation. It is clear from Fig. 2 that because our generator can handle only about 1% PVA (115 000 mol wt) solution, then the viscosity should be kept below about 5 cp. Higher solution concentration can be used if the molecular weight of the polymer is reduced. We observed that for viscous polymer solutions the fluid behaves in a non-Newtonian fashion and the droplets do not undergo clean break-up. Instead, the jet often forms filament-like regions between drops. This effect has been studied by Goldfin et al.[10]

Droplet Generator

The drop generator is the key to the production of large numbers of uniform-sized, high-quality microspheres. The system presently used is based on early designs by Hendricks and coworkers[11-13] although some modifications and improvements have been made for our specific applications.[1]

Our first experiments on PVA were done using the standard droplet generator design.[1] However, we found that the spheres had collapsed into "raisins" (Fig. 3). We also tried a number of methods for adding gases to the sphere during its formation in an attempt to prevent collapse (e.g., blowing agents, solvent mixtures, and various purge gases) but generally with little success. The results of some of these experiments are discussed later.

It was finally decided that the best control of sphere formation could only be achieved by directly adding a low permeability gas to the droplet

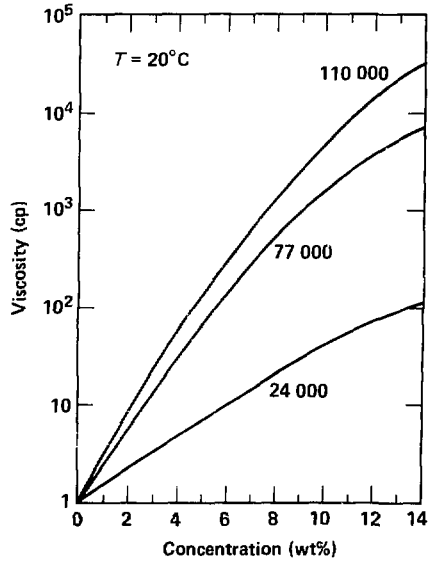

Figure 2. Viscosity of PVA/water solutions for various polymer molecular weights. The data are from Ref. 9.

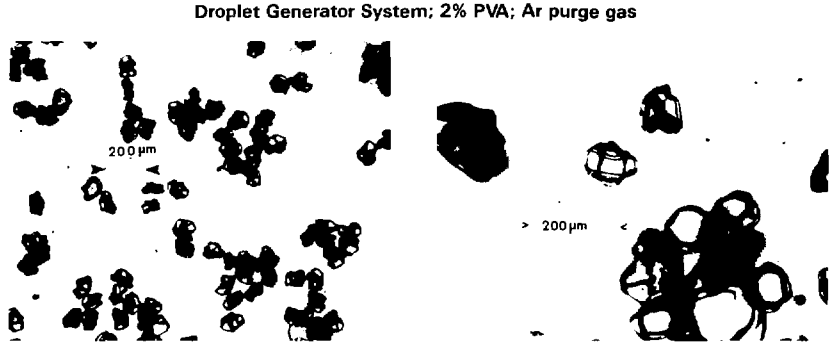

Figure 3. Typical collapsed spheres ("raisins") observed during early PVA microsphere studies using the standard droplet generator design.

as it leaves the generator. This was accomplished using a dual-orifice generator (Fig. 4).

The dual-orifice generator was fabricated using two concentric glass tubes. The inner tube was drawn to a tip having an inside diameter of about 30 μm, whereas the outer tube had a tip i.d. of about 150 μm. For proper operation, the tip of the inner capillary must be located at least 500 μm back from the end of the outer tip (see Fig. 4). Calliger et al.[14] have studied the effects of various parameters on the stable operation of dual-orifice generators and the reader is referred to this work for further details.

During operation, PVA solution is fed to the annulus and the desired gas (argon in most instances) to the inner capillary. The generator operates by producing a uniform-fluid jet that is broken up into droplets by application of a constant-frequency perturbation. The method for break-up of fluid jets was first investigated by Rayleigh[15] and is often referred to as the Rayleigh mechanism. The generator is driven using a piezoelectric ceramic disk mounted along the axis of the outer glass tube (Fig. 4). This drive, coupled with the perturbation produced by the gas bubbles within the liquid stream, provided very stable generator operation.

A photograph of the typical liquid stream break-up is shown in Fig. 5. The generator is being operated at approximately 7500 Hz with a drop size of about 200 μm. The inner gas bubble is about a third to a half the diameter of the drop. Development of the gas bubble at the end of the inner capillary is just barely discernible in Fig. 5(b). In Fig. 5(a), however, one can clearly see the bubble inside the liquid stream just before it exits the generator.

Apart from the generator, the droplet system is comprised of two other parts: a charging ring and a deflection/catcher subsystem. These three components are assembled together on a support stand as shown in Fig. 4. The charging ring is placed below the generator; by applying a positive voltage to the ring, a negative charge is induced on the drop. Any number of drops can be charged by applying a pulse to the charge ring that is both synchronous with the resonator stub and of the proper duration.

The purpose of the charging ring and the deflection/catcher system is to permit the operator to select only a few of the drops to pass down into the drying column. For the PVA work, we generally select about one out of 100 drops. This ratio is purposely large to avoid inter-shell collisions within the column.

The deflection/catcher system (Fig. 4) consists of two electrodes, one of which (the ground electrode) consists of a funnel-shaped tube. During operation, the charged drops are deflected to and caught by the funnel end of the tube and then removed to a waste reservoir by an aspirator. The uncharged drops pass through the deflection region and down into the drying column.

A schematic of the generator system electronics is given in Fig. 6. The sinusoidal output from a Tektronics Model FG501 signal generator is fed to both a variable gain amplifier and Tektronics DD501 event counter. The output from the amplifier (~400 V peak-to-peak maximum) is used to drive the two piezoelectric ceramic disks

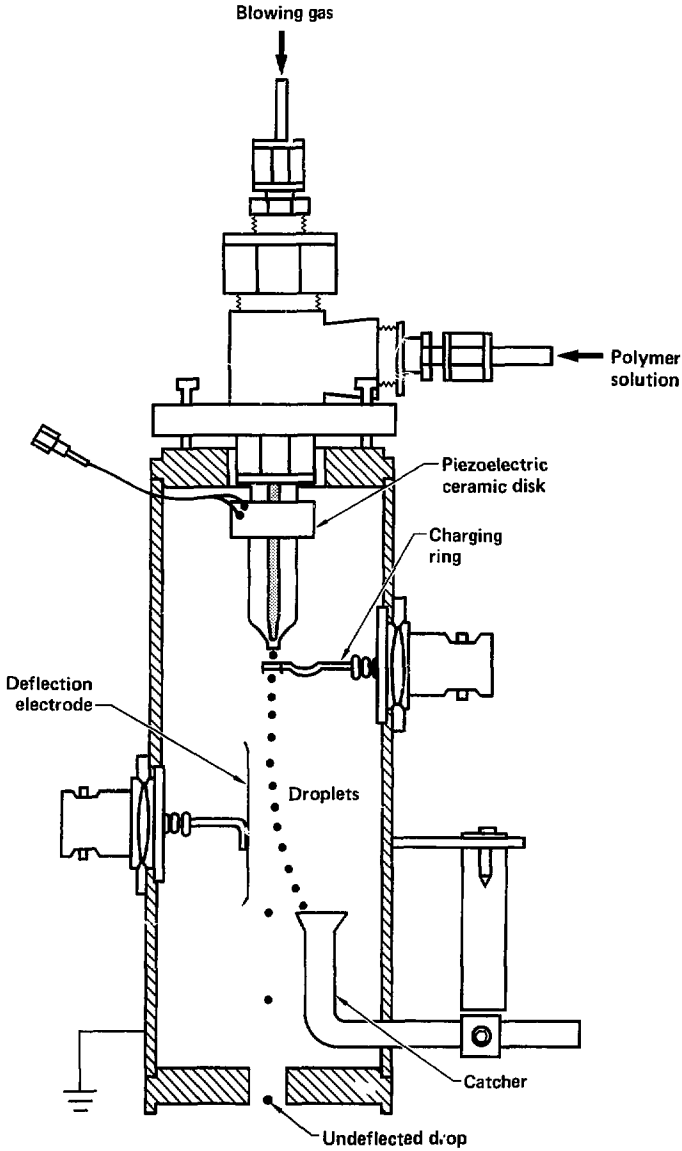

Figure 4. Schematic diagram of the dual-orifice droplet generator used to produce hollow PVA microspheres.

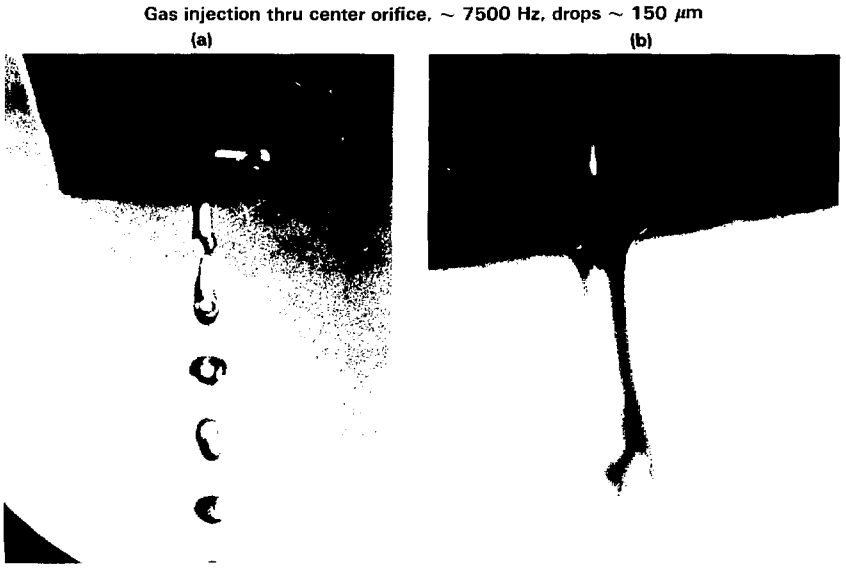

Figure 5. Photograph taken during operation of the dual-orifice generator where the drop size is ~200 μm. Note the gas bubble inside each drop. The generator is operating at ~7500 Hz and the photograph is a 5-s exposure using a strobe light operating at ~100 Hz. Development of the gas bubble at the end of the inner capillary is just barely discernible in Fig. 5(a). However, in Fig. 5(b), one can clearly see the bubble inside the liquid stream just before it exits the generator.

(Vernitron Piezoelectric Division, Type PZT-5A) on the resonator stub. The events counter produces a series of output pulses each equivalent in duration to N cycles of the input. Following N cycles the signal returns to baseline (0.0 V) for the duration of the next cycle.

The output from the events counter goes to a Tektronics PG501 pulse generator that produces the driving signal for both the charging amplifier and the strobe light. A charging voltage of about 220 V is typically used. Note that the signal to the piezoelectric disk is synchronous with that to the charging ring (Fig. 6). The operator can easily change the ratio of charged-to-uncharged drops (the so-called "selection ratio") by simply varying the number (N) on the events counter. The pulse generator is coupled with an LLNL-built delay circuit permitting the operator to fine-tune the width of the charging pulse.

A strobe light is used to illuminate the generator during system tuning and operation. The strobe fires on the leading edge of the 0- to 5-V signal from the pulse generator. Thus, the strobe operates at a frequency of $\nu_g/(N + 1)$ where ν_g is the frequency of the signal generator.

A schematic of the solution feed system to the drop generator is shown in Fig. 7. The polymer solution is driven under pressure from a reservoir, through a millipore filter to the drop generator. The solution feed pressure is maintained constant (~4 to 5 psi ± 0.01 psi) by means of a control loop that uses a Data Instruments Co., model AB pressure transducer located downstream of the millipore filter.

The gas feed to the center orifice is controlled using a needle valve whose pressure on the upstream side is maintained at ~20 psi with a standard gas regulator. Gas flow, started after the liquid flow to the tip is established, is then adjusted until the desired bubble size and drop rate is obtained.

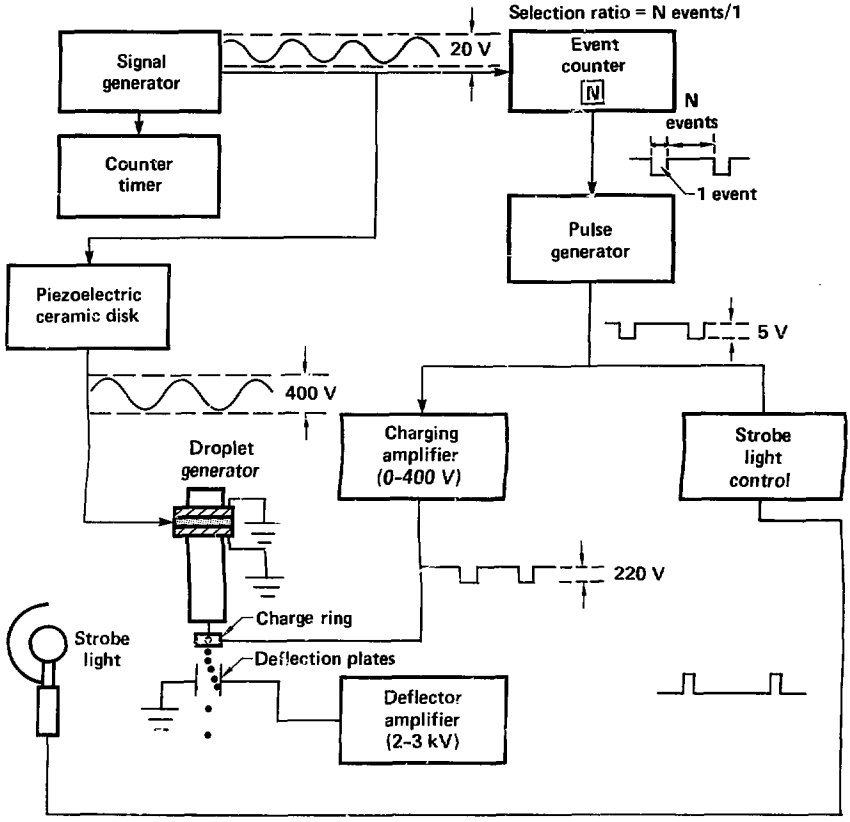

Figure 6. Schematic drawing of droplet generator electronics system.

Drying Column

The heated vertical column used to dry and form the PVA microspheres is shown schematically in Fig. 8. Additional details of the column dimensions and materials are given in Fig. 9. The column design is based largely on the initial PVA drying studies that were carried out at KMSF; the column construction was done jointly by the authors and R. Crawley from KMSF.

The droplet generator sits on top of a collar that caps the drying column. The collar section is long enough to prevent heat transfer to the drop generator thus permitting stable operation for prolonged periods. The droplets pass through a hole in an aluminum plate that supports the generator stand and then drop down into the column.

A purge gas (generally a mixture of helium and argon) is introduced through a port just below the generator and vented at the base of the column (Fig. 8). The purge gas giving the best product is a 80/20 vol% mixture of argon/helium flowing at a rate of about 3 liters per minute (STP). This corresponds to a flow velocity of about

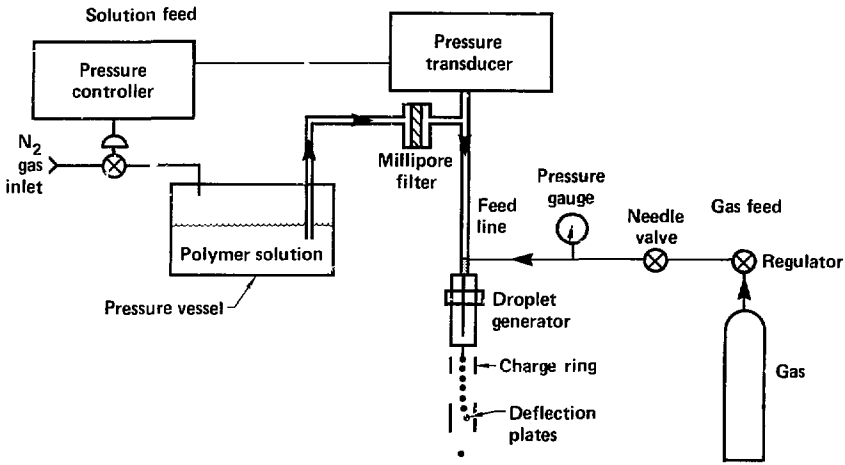

Figure 7. Schematic drawing of the solution and gas feed system.

1 cm/s at STP. The major purpose of the purge gas is to control the heat-transfer characteristics (particularly the thermal conductivity) and hold the axial gas composition constant over extended periods of time. The purge gas also helps eliminate convection currents that may develop in regions where the thermal gradients are largest. The effects of purge-gas heat-transfer characteristics on microsphere formation are discussed in greater detail later in this report (see "Model for Microsphere Formation").

The inlet and exit flow rates must be closely matched to avoid gas going in or out of the hole through which the drops are introduced. We use a wet test meter to accurately balance the flow. Failure to balance the flow rates can change the thermal conductivity of the furnace gas producing a significant deterioration of microsphere quality.

During operation, a large percentage of the product is lost due to collisions with the column wall. Periodically the column is mechanically cleaned to remove any accumulation of material. Note, however, that during a typical run the solids feed rate is less than 1 mg/min so the rate of build-up on the walls is very slow.

The main body of the column is fabricated from two 10-ft sections of glass pipe that have been fused together (Fig. 9). The column is attached to a support structure using a series of clamps located at approximately 4-ft intervals.

The column is heated in 2-ft axial sections. The temperature of each section is controlled using a Fenwal controller with input from a type-K chromel/alumel thermocouple located beneath the heating tape, next to the column wall (Fig. 9). Each section is wrapped with a fiberglass resistance-type heating tape (maximum temperature is approximately 400°C) and insulated with 2.5 cm of Kaowool over-wrapped with aluminum foil tape.

The PVA microspheres are collected in a petri dish that rests on a removable end cap fitted to the base of the column. A high-intensity light, pointed transverse to the column axis, is used to observe the fall of the microsphere near the bottom of the column.

A photograph of the droplet column is given in Fig. 10.

Results from Microsphere Production Experiments

The efforts leading to the development of PVA microspheres occurred in three distinct phases. During the first two phases, we relied on the use of a conventional drop generator and attempted to form hollow microspheres by selecting proper drying conditions and by adding blowing agents. These attempts were highly unsuccessful.

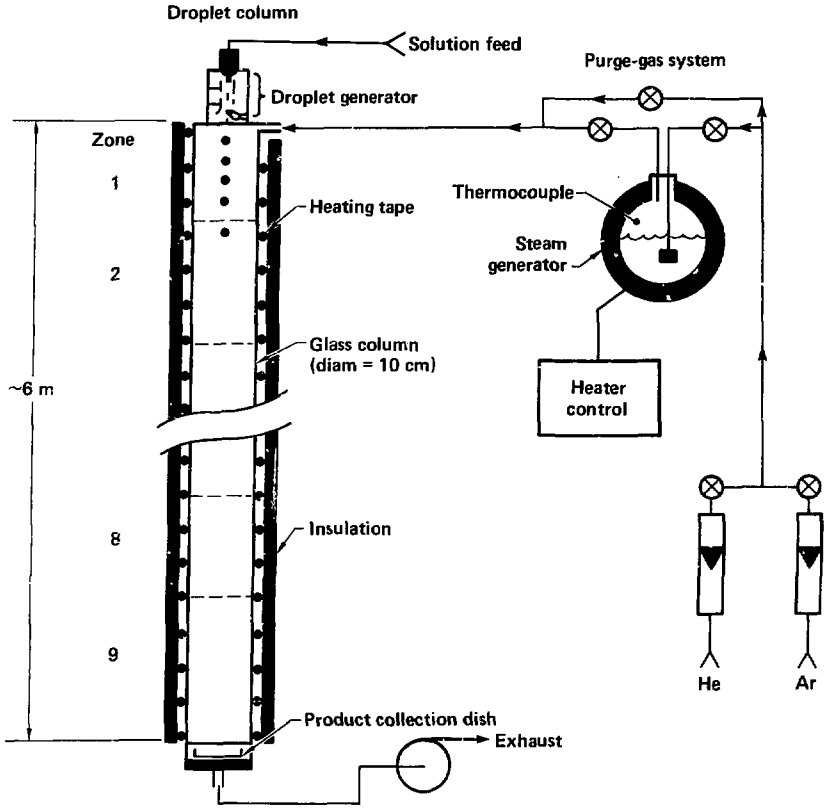

Figure 8. Schematic diagram of drying column and purge gas system.

In the third phase, we developed a dual-orifice generator that produced uniform hollow droplets that, after drying, gave the desired high-quality, hollow PVA spheres.

In the text that follows, the results from the first two phases are briefly discussed since they lead in a logical way to our successful dual-orifice experiments. In parallel with our experimental effort, we also developed a simple 1-D model of the sphere formation process that we used to guide our experimental program. The model development is discussed in detail in a later section of this report. (See "Model for Microsphere Formation".)

Phases I and II: Droplet Experiments with a Conventional Generator

In our first experiments with a conventional generator, we used the standard drying theory to estimate the proper conditions necessary to dry a PVA solution droplet (see Appendix B of Ref. 1) and assumed that this would produce the desired microspheres. However, we found that due to the high permeability of water through PVA, the spheres collapsed into "raisins" as shown photographically in Fig. 3. Figure 11 shows three stages in the droplet drying process that leads to these

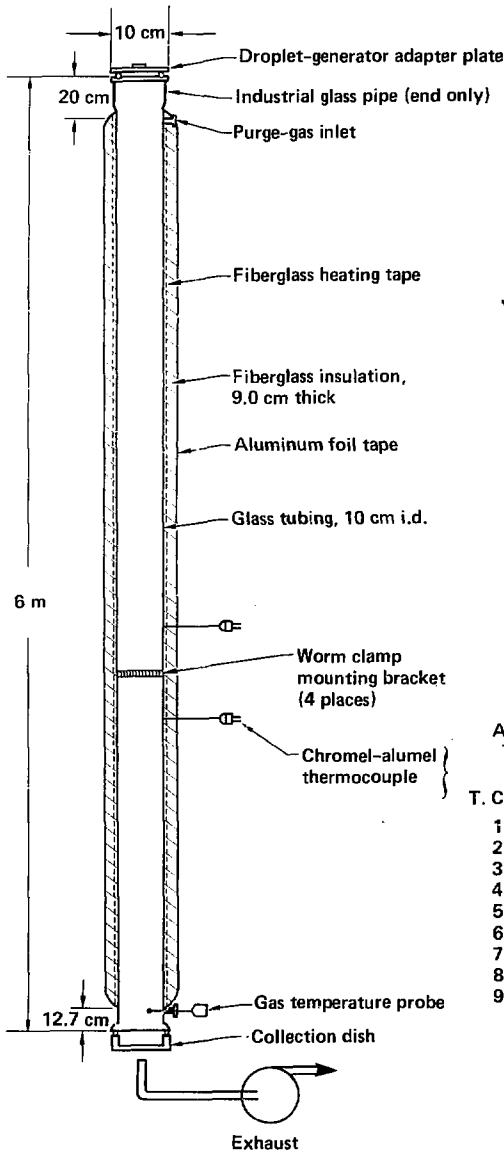

Axial Location of Thermocouples

T. C. #	Distance (cm)
1	71
2	132
3	193
4	254
5	315
6	376
7	437
8	498
9	559

Figure 9. Details of drying column construction showing dimensions and materials.

Figure 10. Photograph of the droplet column and heater control panel.

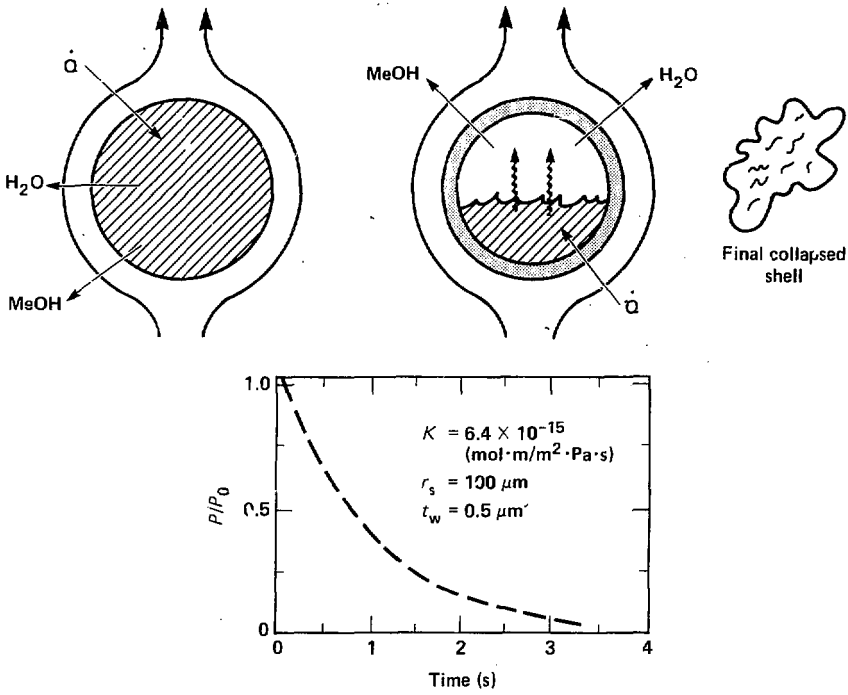

Figure 11. Schematic diagram of PVA/water and methanol droplet showing stages of drying and ultimate sphere collapse that occur in the conventional drop generator. The collapse results from the rapid loss of water and methanol vapor through the shell wall as illustrated in the plot of P/P_0 vs time. See text for details.

collapsed spheres. During the first stage, water and methanol are vaporized from the free droplet surface as heat ($\dot{Q}$) is added from the gas stream. As the solvents are removed, the PVA concentration increases and eventually saturates, forming a skin on the droplet surface. (This occurs at about 35 wt% in water.) During this intermediate stage, the water and the little methanol that remains are vaporized forming a bubble inside the sphere. Unfortunately, the water and methanol gases are rapidly lost through the PVA shell (film) wall and are unable to provide continued internal support once the drop has completely dried. This leads to the formation of a collapsed shell similar to that shown in Fig. 3.

The rapid loss of water through the PVA film is due to its high permeability. This is illustrated in Fig. 11 where the normalized water vapor pressure (P/P_0) is plotted versus time for a 200-μm-diam sphere with a 0.5-μm wall thickness. Using reported values for the water permeability, we have calculated that nearly all the water would be lost from the sphere in about four seconds, a short time compared to the sphere residence time in the drying column (~30 to 60 s), thus causing the sphere to collapse. (In Appendix B of Ref. 1, a set of simple calculations are presented that can be used to estimate drop drying times, fall velocities, and the effects of different column drying conditions on the microsphere formation process.)

It is important to note that the sphere would not collapse if it were outside of the heated column. The strength of PVA at room temperature is sufficient to easily support a 14 psi (1 atm) pressure gradient for a sphere wall thickness of 1 to 2 μm. However, this strength decreases dramatically with rising temperatures; at drying-column temperatures (~200°C), the spheres have essentially zero strength causing them to collapse under a very small pressure gradient.

One possible way to prevent collapse of the microspheres is to reduce the residence time. Unfortunately, this is not practical with our current drying column designs. However, using a commercial spray dryer (Niro model 1) we have been able to dry, remove, and cool PVA microspheres before collapse, but the product size is very small (<50 μm) and nonuniform.

In an attempt to prevent sphere collapse, we tried several methods of adding less permeable gases to the sphere during its formation. These methods can be categorized as blowing-agent techniques and involved the addition of either an easily decomposed salt or a low-permeability solvent to the droplet solution. Of these methods, the one showing the most promise was the use of ammonium carbonate. Ammonium carbonate decomposes at about 60°C producing CO_2 and NH_3. By using 0.5 wt% ammonium carbonate in a 1 wt% solution of PVA, we were able to produce some hollow spheres but they were irregular and often contained gas bubbles in the shell walls. Increasing the drying-column temperature gave some improvement but the spheres were still far from satisfactory (Fig. 12).

Phase III: PVA Microspheres Using a Dual-Orifice Generator

To overcome the problems associated with blowing agents, we decided to use a dual-orifice generator to directly add a low-permeability gas to the droplet. This proved to be the most successful method for producing high-quality PVA microspheres. Scanning-electron microscopy (SEM) photographs of microspheres produced using this method are shown in Fig. 13. Details of the construction and operation of the dual-orifice generator are described earlier in this report (see "Droplet Generator").

The two photographs of collected product in Fig. 14 clearly illustrate the effect of gas addition. The hollow sphere was produced using the dual-orifice generator with gas being added through the center orifice. The collapsed sphere resulted as soon as the gas was shut off.

1% PVA (115 000 mol wt) + 0.5 wt% $(NH_4)_2 CO_3$

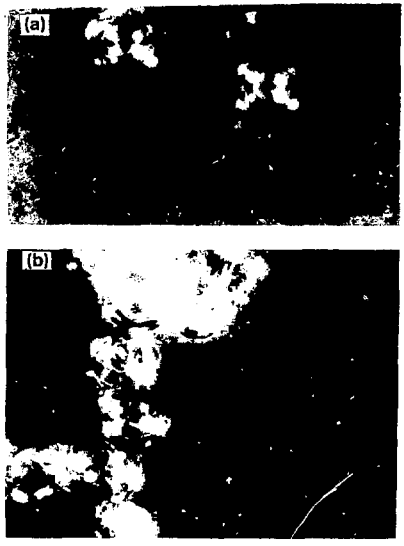

Figure 12. Hollow PVA spheres produced using ammonium carbonate as a blowing agent; (a) shows irregular and (b) shows agglomerated configurations. Note the small gas bubbles in the shell walls.

The best processing conditions for forming good PVA spheres are summarized in Fig. 15. These conditions were developed based on a series of experiments as well as model calculations. The data in Fig. 15 are divided into three parts: (a) the column temperature, (b) the drop generator operating conditions, and (c) the solution composition.

The solution composition is the same as that recommended to us by Downs et al. at KMSF based on their early work. During the course of our work we generally held the solvent composition constant because early tests indicated that solvent changes have an effect on the droplet generator operation. However, we did test the effect of molecular weight. PVA molecular weights of 15 000, 85 000, and 115 000 were tested; good microsphere product was obtained only with the latter two. In general, the 85 000 mol wt PVA is the more desirable of the two; it dissolved easier and gave somewhat improved generator operation.

Figure 13. **PVA microspheres produced using the dual-orifice droplet generator.**

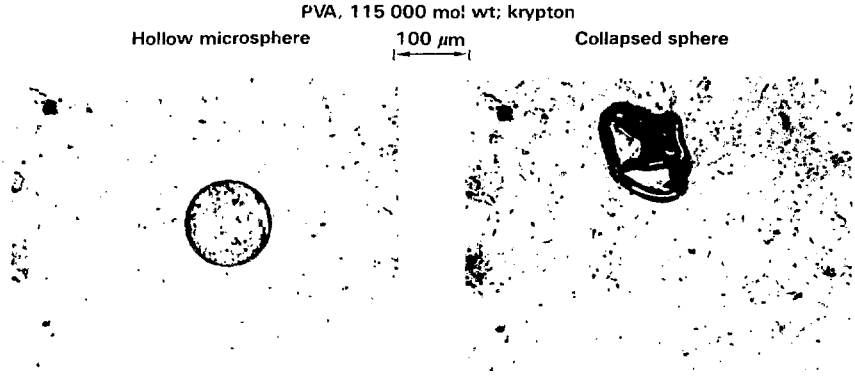

Figure 14. **Product from dual-orifice generator, with and without gas addition through center orifice. Note that without gas addition the sphere collapses.**

The droplet generator conditions were developed largely from empirical observations. We found that droplets in the range of 320 to 350 μm with an inner bubble size of about 1/3 this size produced good quality spheres. Bubble diameters greater than 1/3 the drop diameter generally produced a spectrum of sphere defects, probably due to the very thin walls of the product.

One of the most critical variables in the droplet generator is the selection ratio. This is simply a ratio of the number of spheres that are dropped through the column versus the number produced by the generator. Physically, it represents the spacing between the drops as they enter the column; the higher the selection ratio, the larger the spacing. By keeping the selection ratio high, we dramatically reduce the number of inter-drop collisions in the column. At low selection ratios—i.e., 1/20 to 1/30 (typical of what might be used in our glass microsphere work), there are so many collisions in the PVA system that large droplets form and fall undried through the column. Note that this is a "snow-balling" effect; once one inter-drop collision occurs, the terminal velocity of the resulting drop increases allowing it to overtake and collide with drops (and dried spheres) further down the column. Thus, the size and velocity continues to increase as the drop falls. During our

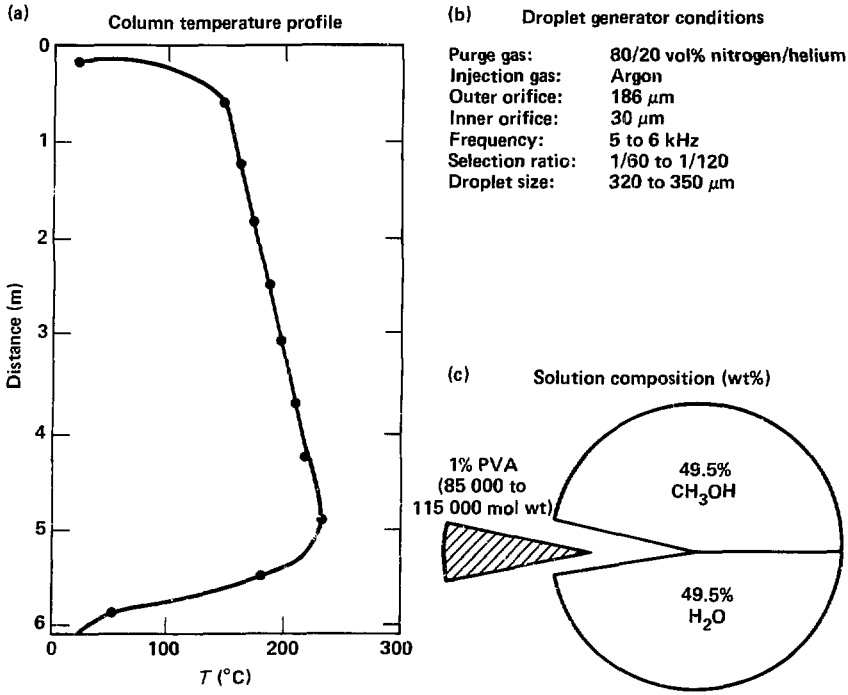

Figure 15. Summary of processing conditions used to prepare PVA microspheres with the dual-orifice drop generator.

experiments, we could see evidence of this by the large drops of "rain" that would fall through the column. Often, partially dried product would be contained within these droplets.

The collision problems within the column are compounded by the low terminal velocities of the dried product. The PVA spheres are typically ~150 to 250 μm in diameter with a wall thickness of only ~1 to 2 μm. Spheres of this size have a terminal velocity of only a few centimeters per second. This low terminal velocity greatly increases the residence time in the column and thus also increases the chance for sphere-to-sphere as well as sphere-to-wall collisions.

Aside from the droplet size and composition, the two other parameters controlling the drying time are the gas thermal conductivity and the furnace temperature. These are related to the drop drying time (t_d) by the approximate equation (see Ref. 1, Appendix B):

$$t_d \simeq \frac{\rho_s \Delta H (D_0^2 - D_f^2)}{8 k_f \Delta T} , \qquad (1)$$

where ρ_s is the solution density (g/cm^3), ΔH the latent heat of the evaporating solvent (cal/g), and D_0 and D_f are the initial drop diameters and diameter at the point of film formation,* respectively. Here, k_f is the thermal conductivity of the gas boundary layer (cal/cm·s·K), and ΔT the temperature drop across the layer; i.e., $\Delta T = T_g - T_s$,

* In Eq. (1), we have not corrected for the injected gas bubble inside the droplet. Since this is only 0.25 to 0.35 times the initial drop diameter, it represents a small fraction of the droplet volume and thus is a minor effect.

where T_g is the purge gas (column) temperature and T_s the adiabatic saturation temperature for the water/methanol mixture.

It is clear from Eq. (1) that drying time can be controlled either by changing the gas composition (consequently changing k_f) or by varying the column temperature or both.

We ran a number of experiments using mixtures of argon/helium and nitrogen/helium as purge gases, and with argon as the bubble injection gas. We added helium for two reasons. First, it has a much greater thermal conductivity than either argon or nitrogen and thus small additions of helium were used to vary the droplet drying rate while holding all other variables constant. Second, the permeability of helium through PVA is much higher than either argon or nitrogen and thus it permeates into the hollow sphere during its fall through the column.

Based on our experiments to date, the purge-gas composition giving the best drying results is an 80/20 vol% mixture of nitrogen and helium. We also found that a mixture of 40/60 vol% argon and helium works almost as well. In all cases, the injected droplet bubble gas is argon.

Increasing the vol% helium in the purge gas also causes an increase in product size (Fig. 16). This is probably due to increased helium permeation into the sphere during its fall through the column.

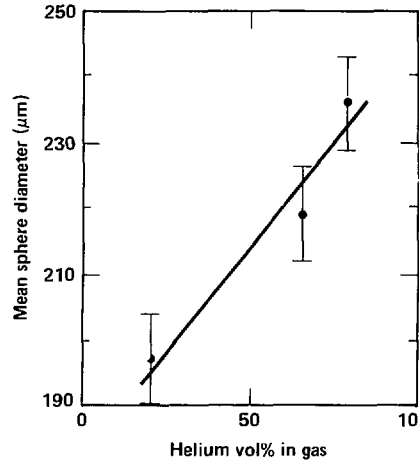

Figure 16. Effect of helium/argon purge-gas composition on final PVA microsphere diameter.

In principle, a number of different column temperature profiles could be used to dry the droplets and form the microspheres. The proper temperatures depend not only on the purge-gas and droplet composition [as related through Eq. (1)] but also on the magnitude of strain that the polymer film can tolerate and the degree of gas diffusion that is required to form the proper sized shell. The temperature profile that we ultimately used is shown in Fig. 15. Note that it gradually increases with distance down the column. This profile was selected based on a combination of the results from our experiments and modeling calculations. The gradual changes in temperature were used to help reduce the high strain rates that occur during the middle stages of drying. Also, by increasing the temperature toward the bottom of the column we increased the rate of helium permeation into the shell as well as increased the PVA strength by slight heat treatment. Further details on why we chose this particular profile are given in the modeling section (see "Model for Microsphere Formation").

Perhaps the greatest problem we faced in preparing PVA spheres was in eliminating the subtle sphere defects that continued to occur. Even though the dual-orifice generator allowed us to make hollow spheres, we were continually plagued by the presence of defects in the sphere surface. Typical examples of common defects are shown in Fig. 17; for the most part, they can be divided into three major categories: (1) large, membrane-like structures that occur from sphere rupture during blowing [Fig. 17(a)], (2) buckling defects caused by collapse during cool down [Fig. 17(b)], and (3) asymmetric shapes due to uneven sphere expansion [Fig. 17(c)]. In addition, we often find incompletely dried spheres as a result of inter-droplet collisions [Fig. 17(d)]; this problem was discussed previously.

To eliminate formation of surface defects requires an understanding of the PVA film rheology at different strain rates and over a wide range of temperatures. To a large extent, the conditions necessary to control defect formation have been determined empirically. We have not yet been able to accurately model these phenomena although work is continuing in this area. The conditions outlined above (Fig. 15) most often give defect-free spheres.

Model for Microsphere Formation

In this section, the major steps in the PVA microsphere formation process are described. In developing this description, we have drawn heavily from the extensive literature on droplet drying (see, for example, Refs. 16–22) and from our own experimental observations. On the basis of this physical picture, a numerical model is then developed that simulates many of the major physical and chemical processes in the microsphere formation process.

Physical Description of Droplet Drying and Sphere Formation

The fate of the hollow droplet after it leaves the droplet generator and enters the heated column is shown schematically in Fig. 18. Note that to a good approximation the process can be divided into two main steps: (1) droplet drying and initial sphere blowing [Fig. 18(a), (b), (c)], and (2) gas diffusion and sphere shrinkage [Fig. 18(d), (e)].

First, consider the drying step. As the droplet leaves the generator, it contains an inner argon gas bubble that is about one-third the sphere diameter and is traveling at an initial velocity of approximately 500 cm/s. This initial velocity is much greater than the terminal velocity and thus the droplet rapidly decelerates. Deceleration occurs over roughly the first meter of column length during which time significant evaporation can occur, particularly if the column is heated.

During the initial stage of drying [Fig. 18(a)], the temperature and solvent flux from the droplet remain approximately constant.[22] The droplet temperature is fixed at the adiabatic saturation temperature defined by the solvent composition, the purge gas composition and temperature. Note that at this stage, the rate of evaporation is in equilibrium with the rate of heat transfer from the surrounding gas. Also, because of its higher vapor pressure and lower latent heat, methanol is lost at a greater rate than water. Thus, the methanol concentration of the solvent decreases.

Eventually the solvent content of the liquid shell diminishes to a point that a PVA film begins to form on the surface [Fig. 18(b)]. This is called the critical point. Based on drying experiments by Marshall et al.,[16–18] film formation begins on the bottom side (leading surface) of the drop, spreads up to the equator and then rapidly closes over the top (trailing surface). The time for the surface film to completely cover the surface is small compared to the time to dry down to that point. Consequently, in our model calculations it is assumed that the surface film forms instantaneously once the droplet reaches the critical concentration.

We have measured the critical concentration for film formation in a series of simple laboratory experiments using the PVA/methanol/water solution. Pools of the 1% PVA solution were dried in air (25°C) over a period of several days. The evaporative mass loss was determined by measuring the sample weight at various times. These data, expressed in terms of the solution concentration and rate of mass loss are plotted in Fig. 19. During the experiment, we recorded the concentration at the first sign of film formation; this occurs at about 17 wt%. Note that due to the added mass-transfer resistance of the film, the rate of mass loss declines significantly beyond this point (Fig. 19).

During droplet drying, the surface film causes the evaporation rate to decline while the heat-transfer rate remains largely unchanged. As a consequence, the temperature of the remaining solvent in the shell begins to increase and ultimately reaches the bubble point of the solvent mixture. The temperature of the droplet remains roughly constant at the bubble point as the balance of the solvent evaporates [Fig. 18(c)]. Most of the vapor from this final solvent evaporation is added to the gas in the inner bubble, causing the hollow droplet to expand into a large hollow sphere. The growth of the sphere at this stage is controlled by the rate with which new material is added to the shell wall and by the rate of vapor accumulation within the bubble (i.e., the difference between the diffusion loss and the evaporation rate). To some extent, the control of this stage is critical. If the drying rate is too high, the strain rate will exceed some critical value and the PVA skin will rupture.

For a fixed solvent system, there are essentially two variables for controlling the rate of drying: the furnace temperature and the thermal conductivity of the purge gas.[22] In our system, we have used both variables to achieve the proper drying conditions to keep the shells intact.

At this point the large, thin-walled PVA sphere enters the second stage of the process shown in Fig. 18(d), and (e). During this stage, the methanol and water vapor solution continues to diffuse out of the bubble at a much higher rate than furnace purge gas diffuses in.

As a consequence, the pressure within the sphere decreases causing the plastic skin to deform. If conditions are properly controlled, the

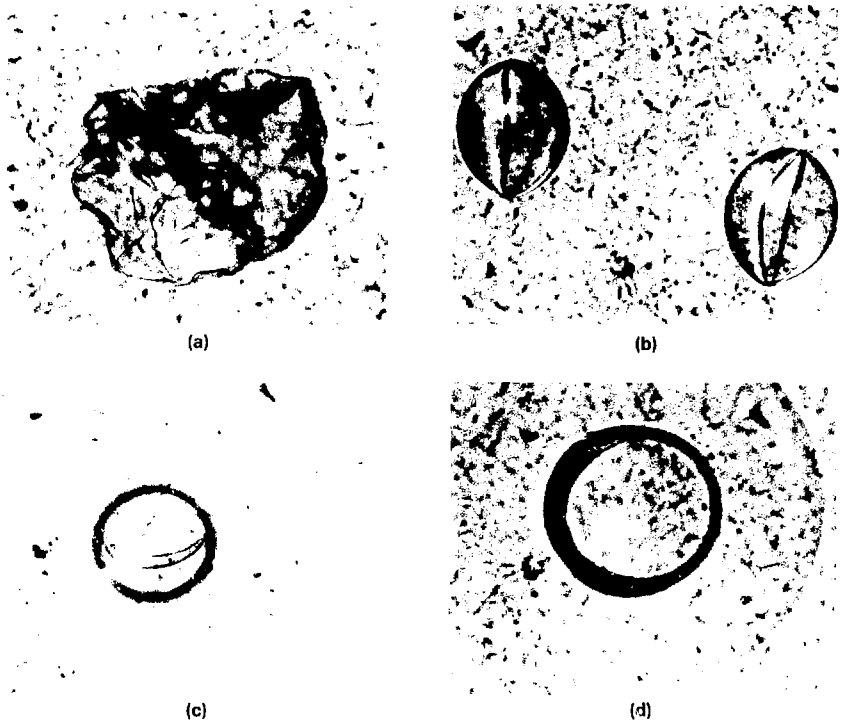

Figure 17. Examples of major types of shell defects observed while preparing PVA spheres using the dual-orifice method.

shell undergoes uniform collapse down to some smaller sphere diameter [Fig. 18(e)]. Note that because of the addition of the low-permeability gas bubble inside the initial drop, the shell does not totally collapse. Instead it shrinks down to a size that depends on the initial bubble size, on the quantity of furnace purge gas that may have diffused into it, and on the column temperature.

The shrinkage/deformation of the polymer shell is controlled by the rheological properties of the polymer. Unfortunately, this step in the process has not been quantified and thus is not included in our model in a detailed way.

As the shell falls through the bottom portion of the column, the temperature decreases and at some point the shell wall becomes rigid. This point determines the final shell diameter.

As the shell cools, the gas pressure within the shell decreases. The residual gas pressure within the PVA shells was measured to be about 0.3 to 0.5 atm. Unfortunately, in the time it takes to complete these pressure measurements, any helium (from the furnace purge gas) has diffused out of the shell leaving only the argon blowing gas. Therefore, this pressure is probably not representative of the final gas pressure of the sphere as it leaves the column.

Mathematical Model

The mathematical model of the shell formation process follows the qualitative description given in the previous paragraphs using well

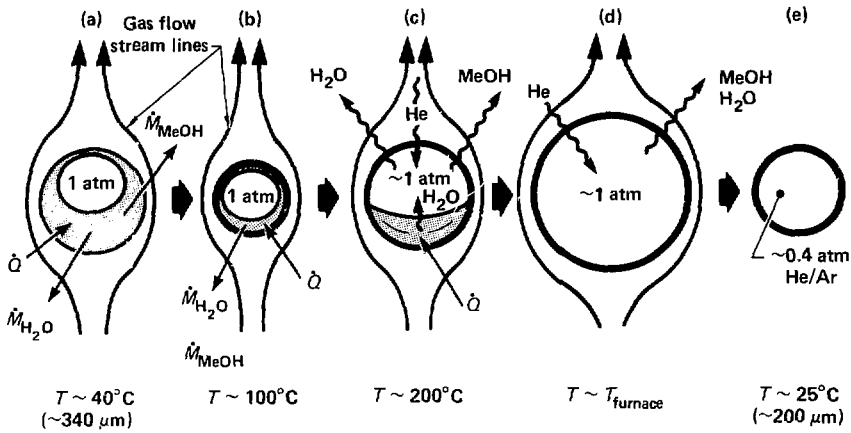

Figure 18. Schematic diagram of various stages in droplet drying. See text for details.

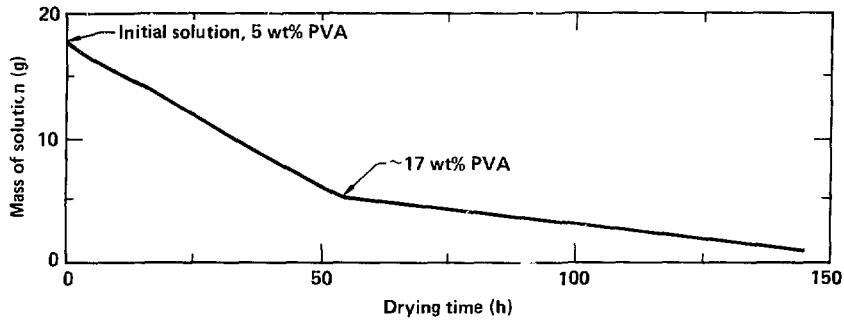

Figure 19. Measured mass loss during evaporative drying of an initial 5-wt% PVA/water solution at 25°C. Film formation occurred at the break in slope of the mass loss vs time curve.

known correlations to estimate required transfer coefficients. For the sake of simplicity, we make the following assumptions:

1. Gas behavior is ideal.
2. Raoult's law holds for solvent mixtures.
3. Drops are spherical and transport properties do not vary with surface location.
4. Films are perfectly elastic and uniform in thickness.
5. Only convective heat transfer is significant.

One additional assumption is made that is probably more important to the calculation than any of those above—we assume film formation over the entire drop surface at some critical polymer concentration. This critical concentration was measured in the laboratory by forced evaporation in air in open dishes, and found to be about 17 wt%. The choice of this value influences the

initial inflation size of the drop and thus the final product diameter. The rather good agreement between observed and calculated product size tends to give some support to the validity of this last assumption.

Droplet Position

Early in the drying process, it is necessary to keep track of the forces acting on the droplet in order to know its velocity and position. The velocity result is used to compute the droplet Reynolds number (Re) and the column position determines the temperature region the droplet is in. The differential equation describing the droplet motion includes the forces due to buoyancy, gravity, and drag:

$$F_b + F_g + F_d = \frac{d(mU)}{dt} , \tag{2}$$

where

$$F_b = V\Delta\rho g \tag{3a}$$

and

$$F_g = mg . \tag{3b}$$

The drag force is computed using the following expression for the drag coefficient, C_d:

$$C_d = \frac{10}{\sqrt{\mathrm{Re}}} , \tag{4}$$

$$F_d = \frac{C_d A_p \rho U^2}{2} , \tag{5}$$

where A_p is the projected particle area and U the velocity. At equilibrium ($d(mU)/dt = 0$) the forces in Eq. (2) all sum to zero.

Equation (2) is used to calculate the initial deceleration of the droplet. Since the initial droplet velocity is known (~500 cm/s), then the time, velocity, and position are calculated by simple stepwise integration.

When the droplet has decelerated to within 2 cm/s of terminal velocity, an explicit calculation is used for terminal velocity,[22]

$$U_t = \left[\frac{4}{225}\frac{(\rho_s - \rho_g)^2 g^2}{\rho_g \mu}\right]^{1/3} D_p . \tag{6}$$

Equation (6) is valid for Reynolds numbers between 0.4 and 500.

Droplet Drying

During the drying phase, the only source of heat for vaporizing the solvent is convective transport from the column purge gas. The rate of mass and heat transfer are in equilibrium, therefore

$$\sum_{i=1}^{n} K_{xm}\,\Delta P_i = h_m\,\Delta T \sum_{i=1}^{n}\left(\frac{X_i}{\lambda_i}\right) , \tag{7}$$

where, for the i^{th} component, ΔP is the difference between the vapor pressure at the particle surface and in the purge gas, X_i is the mole fraction, and λ_i is the heat of vaporization (J/mol). ΔT is the difference between the gas temperature and the droplet temperature. The mass and convective heat-transfer coefficients (K_{xm} and h_m, respectively) are given by[22]

$$K_{xm} = \frac{D_i}{R\,T_a\,D}\left[2.0 + 0.6\,\mathrm{Re}^{1/2}\,\mathrm{Sc}^{1/3}\right] \times \mathrm{g\cdot mol/cm^2\cdot s\cdot atm} , \tag{8}$$

$$h_m = \frac{k_g}{D}\left[2.0 + 0.6\,\mathrm{Re}^{1/2}\,\mathrm{Pr}^{1/3}\right] \mathrm{J/cm^2\cdot s\cdot K} , \tag{9}$$

where D is the diameter (cm), T_a the average temperature across the boundary layer, D_i the diffusion coefficient of the i^{th} component (cm^2/s), k_g is the gas thermal conductivity, and Re, Sc, and Pr are the dimensionless Reynolds, Schmidt, and Prandtl numbers, respectively.

The heat-transfer coefficient, h_m, is corrected for the effect of transpiration at high-mass-transfer rates using the method described by Marshall[20]

$$h_m\,(\text{actual}) = h_m\,(\text{predicted}) \cdot \left(\frac{a}{\exp(a) - 1}\right) , \tag{10}$$

where

$$a = \ln\left[1 + \frac{\mathrm{Nu}}{2}\left(\frac{\Delta T \cdot C_p}{\lambda}\right)\right] . \tag{11}$$

in which Nu is the Nusselt number and C_p is the vapor heat capacity. In our case, h_m (actual) is always 70% or more of the predicted value.

Using gas and vapor properties at the average temperature across the boundary layer, Eq. (7) is solved iteratively for a value of the droplet surface temperature. This value is the adiabatic saturation temperature for the gas/solvent system at the given column temperature.

Thus, an additional integration allows us to calculate the temperature, mass, and composition of the drop as well as its velocity and position during drying.

Blowing a Hollow Shell

As mentioned previously, film formation is assumed to occur at the same concentration as observed in our laboratory drying experiments (Fig. 19). When the film forms, our model assumes that all polymer in excess of that required to maintain the remaining solvent at the critical concentration is distributed evenly over the surface of the growing bubble. At first, this film is quite thin, so its resistance to mass transfer is added to the gas-boundary layer resistance in series. As the film thickens, its resistance dominates and the boundary layer is neglected.

Heat transfer is assumed to take place only to the liquid remaining in a pool at the bottom of the bubble [Fig. 18(c)] and, thus, the area for heat transfer is reduced accordingly. Pressure gradients across the expanding film are considered negligible.

Bubble growth continues until all the solvent is evaporated; this is a relatively short time compared to the time required for a droplet to drop the length of the column. The final calculations are concerned with gas transport through this polymer shell.

Refining the Product Shell

Refining of the initial large PVA sphere [Fig. 18(d)] is treated in our model by simply keeping track of: (1) the gas and vapor fluxes through the shell, (2) the total contained gas volume, and (3) the integrated position (and hence temperature) of the shell in the column. This treatment is an oversimplification because it does not include the rheology of the polymer film during shrinkage of the large thin-walled sphere down to final product. This is currently the greatest weakness of the model because it does not allow prediction of failure or defect formation. As discussed previously, we experimentally found that most defects occur during this stage of the process.

The gas flux through the shell is computed from the permeability of the shell and from the shell wall thickness. The permeability (K_p) is assumed to have the form:

$$K_p = A_k \exp(B/T) \ , \qquad (12)$$

where A_k and B are constants and T is the temperature. Such a relation works quite well for simple gases, but is not correct for solvent vapors that swell the polymer matrix and exhibit concentration dependent behavior (as is the case for water permeability in PVA). We use Eq. (12) in this work as an expedient, until better data become available.

The final size of the product sphere is the only real data against which the calculation can be normalized. The permeabilities reported in the literature range over more than an order of magnitude, and values within that range can be selected that allow the calculation to match the experimentally observed product.

As mentioned above, the primary limitation in our present model is its inability to predict and treat defect formation. One variable that we have found useful in analyzing failure modes is the surface strain rate; note that the surface strain rate is positive during initial blowing and generally negative during the refining stages. We have found that failures involving rupture of the shell are related to high, positive strain rates, while denting and crumpling are related to high negative rates. A primary use of this part of our model calculations has been to predict the effect of temperature profile changes on strain rate. The profile used for our current shell production has an increasing temperature ramp during refining of the initial bubble and is an attempt to minimize both the rate and magnitude of surface strain.

Results from a typical model calculation showing droplet drying and microsphere formation are given in Fig. 20. We plotted the droplet diameter, velocity, and temperature as a function of distance down the column. We also added to the calculation the temperature profile of the drying column.

We clearly see in Fig. 20 the stages of drop drying and sphere formation that were described earlier. The velocity plot shows the period of deceleration as the droplet leaves the generator and also the rapid decrease in terminal velocity once the sphere starts to inflate. Similarly, the calculated drop diameter as a function of distance down the column illustrates the three stages of (1) drop dry-down to film formation, (2) sphere blowing, and (3) sphere shrinkage caused by gas diffusion. Note that in the case of sphere shrinkage the model predicts only partial collapse down to some inner gas volume. This is because a bubble of low-permeability gas has been added, without which the shell collapses completely down to a solid particle.

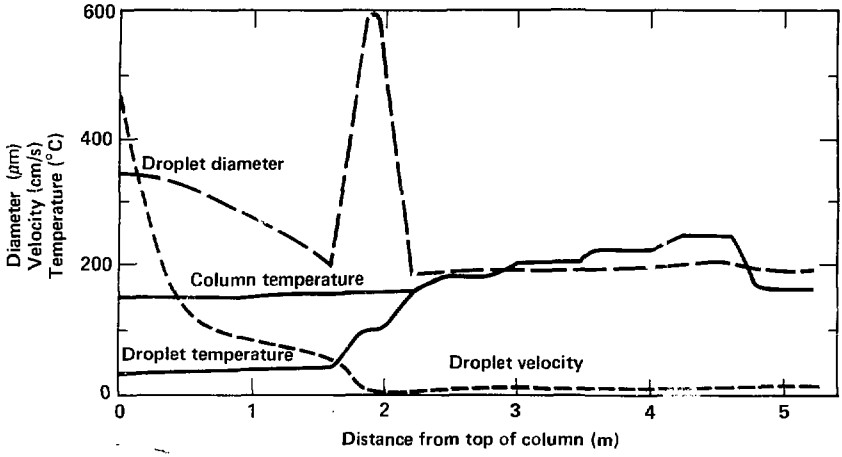

Figure 20. Results from model calculations simulating drying of a hollow droplet as a function of distance down a heated column. The plots show the droplet diameter, temperature, and velocity at various stages of the drying process. Also shown is the furnace temperature profile that was included in the calculations. These results are for the standard operating conditions that gave good quality PVA spheres (see Fig. 13).

Properties of PVA Microspheres

We discuss here the physical properties of PVA, much of which is taken from the rather extensive literature available on this polymer (see, for example, Refs. 9 and 23 to 26). When data have not been available for certain properties; we have developed specific tests to measure these properties.

In most of our work, two different average molecular weights of PVA have been used: 115 000 and 85 000. Both are greater than 99% hydrolyzed and were obtained from a commercial source (Aldrich Chemical Co.). Nominal values reported for many of the key physical properties are summarized in Table 2. In the pages that follow, certain PVA physical properties of importance to ICF applications are discussed in greater detail.

Note that many of the PVA properties change significantly in the pressure of small amounts of water vapor.[9] Therefore, in handling PVA microspheres or in measuring physical properties, close attention should be given to either exclude water vapor or to control it at some known level. This is particularly important for films since the equilibrium moisture content of the PVA increases dramatically with small increases in water-vapor pressure (see Fig. 21).[9]

Thermal Stability

When heated in a vacuum or in an inert gas, PVA begins to degrade at about 200°C at a heating rate of 10°C/min (Fig. 22). Higher heating rates will cause this to shift to higher temperatures. (Because the degradation is kinetically driven, the degree of reaction will depend on the time at a given temperature. Thus the TGA, DTG, and DSC data given here at 10°C/min may not be representative of other heating conditions.)

The thermogravimetric analysis (TGA) data show three distinct regions of mass loss: (1) 50 to 100°C, (2) 200 to 350°C, and (3) >400°C [Fig. 22(a) and (b)]. In the first region, about 4% mass loss results from evolution of free water absorbed in the polymer. This moisture loss agrees well

Table 2. Nominal values for several key physical properties of dry PVA. Note that many properties are affected by the presence of small quantities of water vapor.

Properties	
Structure	$(-CH_2CH(OH)-)_n$; n = 1900 to 2000
Mean molecular weight	85 000 to 115 000
Mean atomic number (Z)	3.43
Density (g/cm^3)	1.27
Refractive index	1.49 to 1.53
Composition	
Carbon	28.6 at.% 54.5 wt%
Hydrogen	57.1 at.% 9.1 wt%
Oxygen	14.3 at.% 36.4 wt%
Thermal properties	
Heat capacity ($cal/g \cdot K$)	0.36
Thermal conductivity ($J/s \cdot m \cdot K$)	0.16 to 0.20
Linear expansion coefficient ($cm/cm \cdot K$)	1×10^{-4}
Glass transition temperature (°C)	99
"Melting" point (°C)	258[a]
Mechanical properties	
Elastic constants	
Young's modulus ($\times 10^6$ psi)	1.1
Bulk modulus ($\times 10^6$ psi)	1.8
Shear modulus ($\times 10^6$ psi)	0.39
Poisson's ratio	0.4
Compressive strength ($\times 10^3$ psi)	13 to 22
Tensile strength ($\times 10^3$ psi)	8.8 to 15
Flexural strength ($\times 10^3$ psi)	13 to 22

[a] Decomposes rapidly above 200°C.

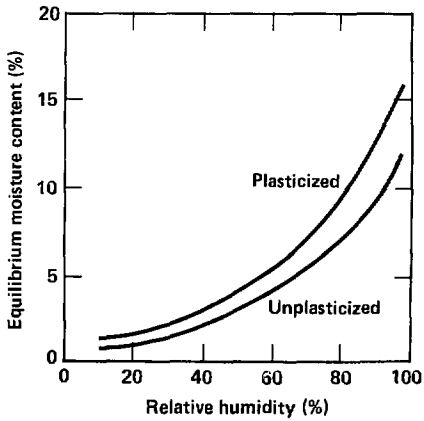

Figure 21. Equilibrium moisture content in plasticized and unplasticized PVA film as a function of relative humidity at 20°C. Data are from Ref. 9. The water vapor pressure at 100% humidity is 0.023 atm.

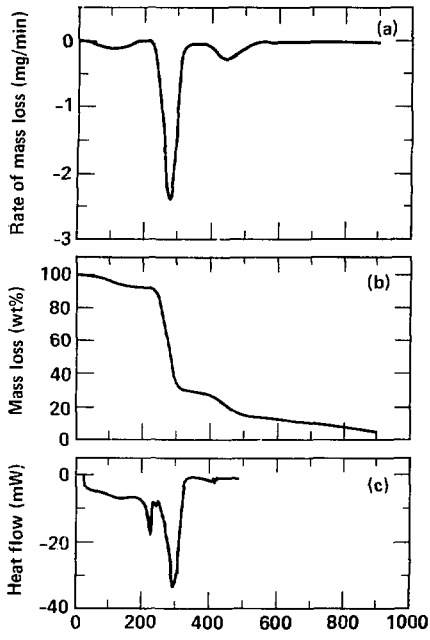

Figure 22. (a) Rate of mass loss and (b) mass loss as a function of temperature for PVA powder (85 000 mol wt) heated at a rate of 10°C/min in nitrogen. (c) Heat flow in PVA (115 000 mol wt) as measured by differential scanning calorimetry between 20° and 480°C.

with what one would predict for a sample stored at 60% relative humidity at 20°C (see Fig. 21); this sample was stored in room air prior to testing.

Between 200 and 350°C, PVA loses about 80% of its mass. Because this mass loss is so large, it is clear that it does not originate from only one degradation reaction. For example, the splitting off of all the hydroxyl groups (as H_2O) would produce a mass loss of about 40%. It is reported that between 100 and 250°C, PVA degradation involves primarily the splitting off of water. This often leads to a distinct yellow coloration in the product. At higher temperatures (~250 to 300°C), the decomposition products are aldehydes, ketones, and hydrocarbons. Above this primary pyrolysis region (i.e., $T > 350$°C), the remaining carbonaceous residue undergoes still further decomposition and is reported to release CO and aromatic hydrocarbons.[9] Undoubtedly some evolution of CH_4 and of H_2 occurs as well.

Radiation Stability

One of the recurring questions associated with the preparation of polymeric microspheres is the degree of damage caused by ionizing (β) radiation from the tritium decay. In the text that follows, we present a brief discussion on the probable effects of damage on polymer shells followed by results from simulated damage tests on PVA and other potential polymer shell candidates.

Several excellent reviews and text books[27-33] discuss the effects of radiation damage on polymers. As a consequence, we will not present here details of the damage mechanisms. There are, however, several key points and rules of thumb to bear in mind.

First, organic polymers are very susceptible to structural damage by α and by low-energy β radiation (<0.3 to 0.4 MeV) whereas inorganic glasses are not. In general, the mechanical properties of polymers begin to degrade at doses as low as 10^6 to 10^7 rad and very few polymers are usable at doses greater than 10^9 rad.[27,32,33]

Second, radiation-induced changes in organic materials are selective, i.e., they depend strongly on the functional group types in the polymer. For example, aromatic compounds are relatively stable to radiation and, thus, the presence of aromatic groups in the polymer structure enhances stability. On the other hand, compounds containing halogens are relatively susceptible to radiation damage; consequently, polymers containing halogens can be expected to degrade quite rapidly. Also, among the aliphatic polymers the unsaturated species (containing double or triple bonds) are less stable than the saturated species. Table 3 (Ref. 33) and Fig. 23 (Ref. 27) summarize radiation damage data for a number of common thermoplastics.

A third point to keep in mind is that at high damage levels some gas evolution will occur due to the dissociation of small side groups from the main polymer chain. A summary of reported gas yields[27] for several polymers is given in Table 4. In most cases, even severe damage would release only enough gas to produce about 1 vol% contamination of a typical DT fill, a level that may not be significant enough to affect the performance of the fuel. In the case of targets stored

Table 3. Effects of radiation on selected thermoplastic polymers (from Ref. 33).

Polymer	Radiation stability	Radiation dose to produce significant damage (Mrad)
ABS	Good	100
Acetals	Poor	1 to 2
Acrylics		
PMMA	Fair	5
Others	Fair	10
Amides		
Aliphatic	Fair	50 to 100
Aromatic	Excellent	1000
Cellulosics	Fair	20
Fluoroplastics		
PTFE	Poor	1
PCTFE	Fair	10 to 20
FEP	Fair	20
PVF,PVF_2,PETFE	Good	100
Polycarbonate	Good	100
Polyesters (aromatic)	Good	100
Polyolefins		
Polyethylene	Good	100
Polypropylene	Fair	10
Polymethylpentene	Good	30 to 50
Copolymers	Good	50
Polystyrene	Excellent	1000
SAN	Good	100 to 500
Polysulfones	Excellent	1000
Polyvinyls		
PVC	Good	50 to 100
Copolymers	Fair	10 to 40

under cryogenic conditions (to lower leakage via diffusion), gas may be generated and trapped in the polymer structure only to produce bubbles upon subsequent heating.[27]

One final area of concern is the potential exchange of tritium for hydrogen in the polymer structure. Exchange of hydrogen in the polymer wall could produce a significant reduction of tritium concentration in the fill gas.

Severe radiation damage of a given polymer produces changes in most physical properties. There is often a dramatic reduction in mechanical strength, changes in electrical properties, emission of gas products, and, in many cases, visible deterioration of the surface (bubbling, cracking, etc.).

For the case of tritium decay, the average β energy is about 7 keV and the corresponding depth of penetration in a typical polymer is 1 μm. Because the polymer shells for ICF experiments will have wall thicknesses much greater than 1 μm, a loss of strength in the first micron may not be a problem. Likewise, changes in other physical properties such as elastic moduli and electrical properties may be unimportant. On the other hand, any physical deterioration of the shell-surface quality will probably be unacceptable.

With the realization that radiation-induced changes in surface quality are perhaps the most immediate concern, we have examined the effects of β radiation on polymer shell-surface quality. Rather than use DT in this first phase of our study, we have simulated the β radiation using the 7- to 10-keV electron beam of a scanning electron microscope (SEM) (Fig. 24). Using the SEM has advantages and disadvantages. The advantages are:

1. The degree of surface deterioration as a function of time (dose) can be directly observed via the SEM image.
2. Very large doses can be given in rather short experimental times.
3. The difficulties and high cost associated with DT handling are eliminated.

On the other hand, the major disadvantages are:

1. Any radiation-induced reactions of the polymer with hydrogen cannot be simulated.
2. The dose rate is much greater than that experienced under real fuel handling conditions. Therefore, if the extent of damage depends on the *rate* as well as the total dose then these tests may exacerbate the damage.

Estimates of Radiation Damage to a Polymer Microsphere

Estimating the radiation damage to a polymer shell in a given time requires that we calculate the mass of polymer exposed and the rate of β emission by the DT. For tritium decay, the average β energy is about 7 keV* corresponding to a range (R_b) of 1×10^{-4} g/cm^2. The average penetration depth (X_p) can be calculated from the range and the material density (ρ, g/cm^3)

$$X_p = R_b/\rho \ . \qquad (13)$$

For example, a typical polymer has a density of about 1.0 g/cm^3 corresponding to an average penetration depth of about 1 μm. Similarly, the average penetration through a 0.01 g/cm^3 DT fill is estimated to be 100 μm.

The mass of polymer exposed (m_p) is calculated from the penetration depth (X_p) in the polymer

$$m_p \simeq 4\pi r_s^2 X_p \rho_p \quad ; \quad \text{for } X_p \ll r_s \ , \qquad (14)$$

* The distribution of β energy is rather broad (and unsymmetrical) with a maximum energy of nearly 18 keV. The average is about 40% of the maximum or 7 keV.

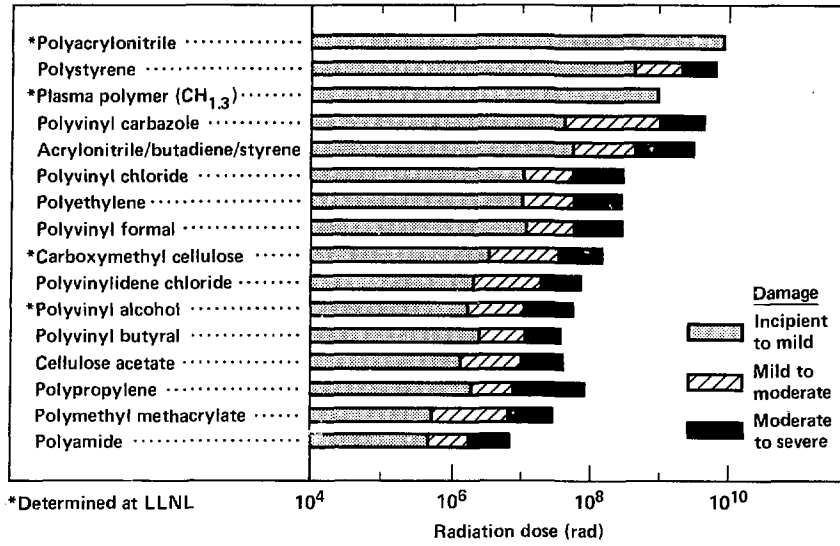

Figure 23. Radiation damage data for several thermoplastics. These data are from Ref. 27 as well as e-beam tests at LLNL. The LLNL tests are based on observed deterioration of surface quality only. It is likely that deterioration of other properties will occur at lower doses.

Table 4. Gas yields from polymers irradiated at 20°C in air (from Ref. 27).

Polymer	Gas evolution rate cm^3 (NTP)gm^{-1} $Mrad^{-1}$	G-value[a]
Low-density polyethylene	0.09	3.86
High-density polyethylene	0.07	3.06
Polystyrene	0.0006	0.026
Plasticized PVC	0.027	1.16
Unplasticized PVC	0.018	0.77
Polymethyl methacrylate	0.027	1.18
PTFE	0.0022	0.098
Nylon 6	0.024	1.02
Polycarbonate	0.020	0.86
Polyethylene terephthalate	0.004	0.17
Polyimide	0.00006	0.0026
Epoxide resins (a range)	0.0029 to 0.13	0.12 to 0.57

[a] G-value = number molecules of gas produced per 100 eV of energy deposition.

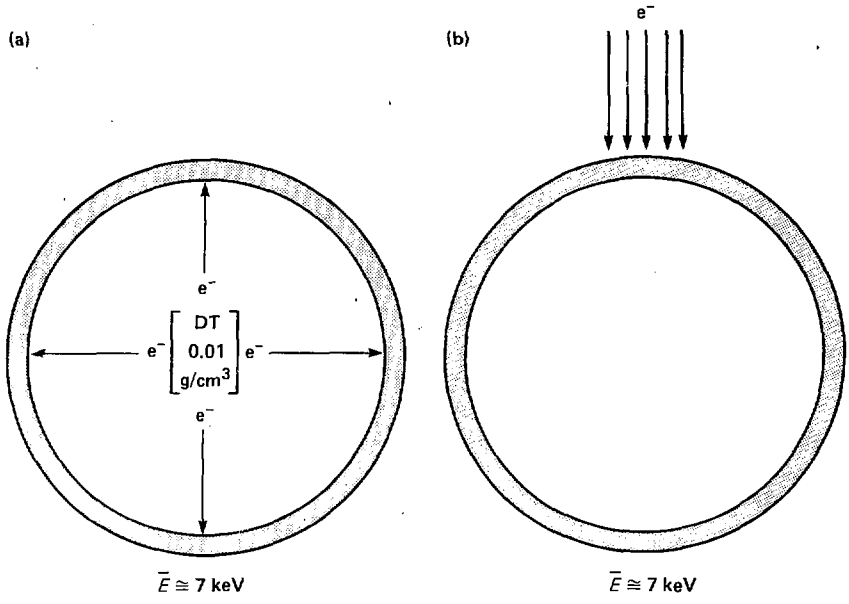

Figure 24. (a) Schematic diagram of a polymer shell subjected to β irradiation from a 0.01 g/cm^3 DT fill. For a nominal 200-μm i.d. shell, this corresponds to an energy flux of about 500 keV/μm^2·s. (b) Simulated β irradiation using the SEM 7-keV electron beam; typically an energy flux of about 1.6 × 10^5 keV/μm^2·s was used.

where ρ_p is the polymer density (g/cm^3) and r_s the shell radius (cm).

The β radiation that strikes the polymer wall originates within a source volume defined by the penetration distance through the DT (Fig. 25). The number of tritium atoms within this source volume is then simply:

$$N_T = \frac{4\pi \rho_{DT} N_A}{3M_{DT}} \left[r_s^3 - (r_s - X_D)^3\right] , \quad \text{for } X_{DT} \le r_s , \tag{15a}$$

$$N_T = \frac{4\pi \rho_{DT} N_A r_s^3}{3M_{DT}} , \quad \text{for } X_{DT} > r_s , \tag{15b}$$

where X_{DT} is the average penetration distance (cm) through a DT fill of density ρ_{DT} (g/cm^3), N_A is Avogadro's number and M_{DT} the molecular weight of DT (g/mol).

The rate of β emission from within the source volume is

$$\frac{d\beta}{dt} = \frac{\ln 2}{t_{1/2}} N_T , \tag{16}$$

where $t_{1/2}$ is the half life of tritium (12.3 y).

Combining Eqs. (13) to (15) and multiplying by the average β energy (E_β) gives the rate of energy deposition per gram of polymer:

$$\frac{dE_D}{dt} = f_c \frac{E_\beta N_T \ln 2}{t_{1/2} m_p} . \tag{17}$$

Included in Eq. (17) is a correction factor, f_c, that accounts for (1) the β particles that are emitted in a direction away from the shell wall and (2) the partial self-shielding effects of the DT within the source volume. A more detailed calculation of f_c

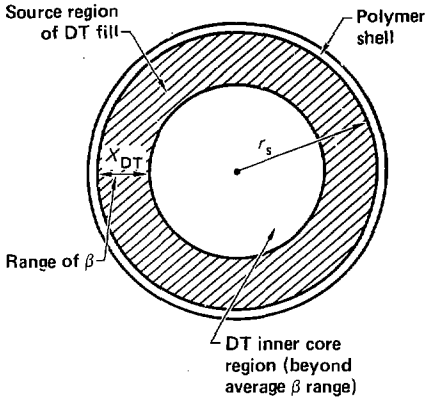

Figure 25. Schematic diagram of a DT-filled polymer shell of radius r_s. The hatched region represents the zone of the DT fill that provides a source of β radiation hitting the polymer wall; the thickness of this zone is equal to the penetration depth (X_{DT}). Beta radiation from the very inner core of the DT will not have sufficient energy (on the average) to penetrate to the wall.

could be made but is not justified for these particular experiments.

A plot of the rate of energy deposition as a function of shell radius and fill density is shown in Fig. 26. The parameter values used in these calculations are summarized in Table 5. For very large shell radii, the energy deposition rate approaches a limiting value ($\sim 1.36 \times 10^{18}$ keV/g·h = 21.7 Mrad/h) that is independent of density.

From the curves in Fig. 26, it is possible to estimate the fuel container lifetime provided radiation damage information exists for the particular shell polymer. An example of such data for several common thermoplastics is given in Fig. 23 (Ref. 27) and in Table 3 (Ref. 33). From these data it is clear that polystyrene would make an excellent shell choice (on the basis of radiation stability) because it can take as much as 10^3 to 10^4 Mrad before severe damage. On the other hand, polymethyl methacrylate would make a poor choice since severe damage occurs after an exposure of only 10 Mrad or less than one hour for our particular application (see Fig. 26).

Description of Irradiation Tests

Because we were unable to find radiation stability data for polyvinyl alcohol, we carried out irradiation tests on this polymer using a 7- to 10-keV electron beam.

Besides PVA, several other polymers that are possible candidates for polymer shells were also irradiated. Table 6 summarizes the polymers used and their source, method of preparation, etc. All the materials were either hollow spheres or a coating (i.e., CH) on a sphere, and the sizes were generally in the 100- to 250-μm-diam range.

The spheres were mounted on plastic transfer adhesive and then overcoated with 150 to 200 Å of carbon. (Without a thin conductive carbon coating the spheres soon charge up to such an extent that the beam current to the sample drops dramatically.)

The samples were irradiated at a current of about 10 picoamps and an electron beam energy of 7 or 10 keV using a Cambridge Stereoscan 180 SEM. During the experiment, photographs of the SEM scan image were periodically taken to record changes in surface quality.

The total radiation dose (D_R) to the sample was calculated from the expression

$$D_R = 1.0 \times 10^{-2} \frac{i_b E_b t}{A_s \rho_p X_p}, \qquad (18)$$

where i_b is the current (e /s),* E_b energy of the SEM beam (erg), t the exposure time (s), A_s the scan area (cm^2), X_p the penetration depth of the electron in the polymer (cm), and ρ_p the polymer density (g/cm^3). The factor of 0.01 is to convert the dose from erg/g to rads. Table 7 summarizes the experimental conditions for the irradiation experiments and the calculated *cumulative* dose (Mrad). In many of the experiments, photos of the surface

* 1 amp = 6.24×10^{18} e /s.

Table 5. Summary of parameter values used to calculate the energy deposition rate via the method outlined in the text.

$f_e = 0.25$
$\rho_p = 1.0$ g/cm^3
$M_{DT} = 5$ g/mol
$N_A = 6.023 \times 10^{23}$ molecules/mol
$R_p = R_{DT} = 1 \times 10^{-4}$ g/cm^{-2} at 7 keV
$t_{1/2} = 1.078 \times 10^5$ h
$X_p = 1 \times 10^{-4}$ cm
$E_\beta = 7$ keV

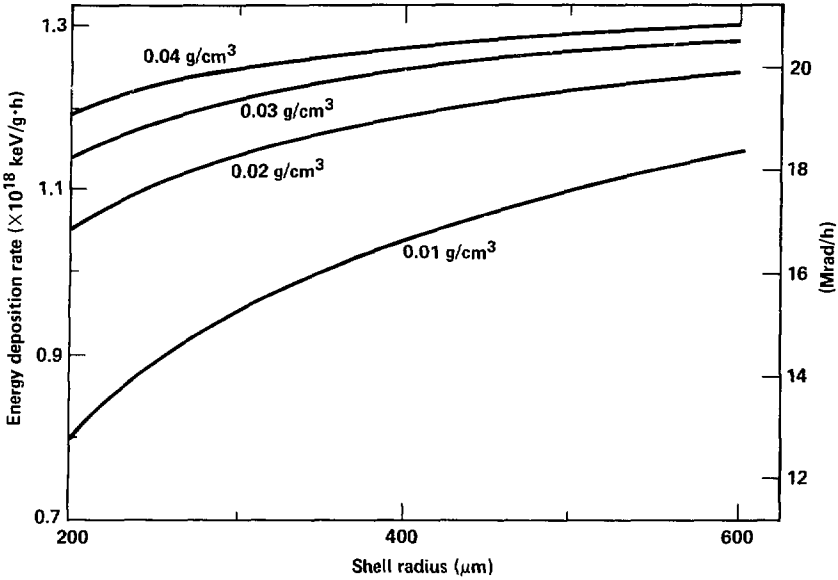

Figure 26. Plot of energy deposition rate as a function of shell size and of DT-fill density.

Table 6. Source of polymer shells used in electron-beam irradiation tests.

Material	Prep. sample No.[a]	Shell/coating prep. method	Polymer source	Average mol wt.	Monomer structure
Polyvinyl-alcohol	JP-52 (LLNL)	Droplet column	Aldrich Chemical	115 000	$-CH_2CH(OH)-$
Polyacrylo-nitrile	DGDC47C (KMSF)	Droplet column	Dupont type 7	100 000	$-CH_2CH(CN)-$
Polystyrene	3384-66[b] (KMSF)	Droplet column	Unknown	Unknown	$-CH_2CH(\phi)-$
Carboxymethyl-cellulose	SD30223B (LLNL)	Spray dryer	Hercules CMC (7M8)	250 000	Cellulose related
Plasma coated CH	HRC series (LLNL)	R.F. Plasma polymerization	LLNL[c]	Unknown	Unknown

[a] The letters in parentheses denote whether the shells came from KMSF or LLNL.

[b] Assigned LLNL #B270.

[c] Prepared by S. Letts/R. Corley at LLNL.

Table 7. Summary of radiation damage test conditions and dose.

Material	Sample No.	Beam Energy keV	Beam Energy erg($\times 10^{-6}$)	Current ($\times 10^{-12}$ amps)	Total exposure time(s)	Area ($\times 10^{-5}$ cm^2)	Density (g/cm^3)	Dose (Mrad)	Surface damage
Polyvinyl-	RS-3A	10	1.60	10.0	900	2.51	1.27	2800	Severe[a]
alcohol	RS-4A	7	1.12	10.2	80	2.50	1.27	180	Visible damage
	RS-10A1	7	1.12	10.0	80	2.50	1.27	176	Visible damage
	RS-10A2	7	1.12	10.0	32	2.50	1.27	70	Visible damage
	RS-14A	7	1.12	10.0	900	2.50	1.27	1981	Severe
	RS-14B	10	1.60	10.0	900	2.50	1.27	2830	Severe
	RS-14C	7	1.12	10.0	240	0.45	1.27	2930	Severe
	RS-14D	10	1.60	10.0	600	0.45	1.27	10500	Severe
Polystyrene	RS-3B	10	1.60	10.0	900	2.51	1.06	3370	None visible
	RS-4B	7	1.12	10.2	1055	2.50	1.06	2840	None visible
	RS-10B	7	1.12	10.0	1900	2.50	1.06	4750	None visible
Polyacrylo-	RS-4C	7	1.12	10.8	230	2.50	1.18	590	None visible
nitrile	RS-10C1	7	1.12	10.0	1600	2.50	1.18	4260	None visible
	RS-10C2	7	1.12	10.0	5400	2.50	1.18	12800	None visible
Plasma	RS-4D	7	1.12	10.8	390	2.50	1.0	1180	None visible
coated CH	RS-10D	7	1.12	10.0	1800	2.50	1.0	5030	None visible
Carboxymethyl-	RS-15	7	1.12	10.0	1200	2.50	1.59	2110	Severe
cellulose	RS-16	7	1.12	10.0	1200	2.50	1.59	2110	Severe

[a] The term "severe" implies many large-scale defects (>3 μm) and/or cracks.

were also taken at intermediate times thus showing the evolution of damage with increasing dose.

Results from Irradiation Tests

In all the tests, PVA and carboxymethylcellulose (CMC) showed evidence of some surface damage even for total doses as low as 30 and 100 Mrad, respectively. A typical example of severe damage to PVA (dose ~3000 Mrad) is shown in Fig. 27. Figures 27(b) and (c) are of the same exposed surface on PVA showing development of surface defects about 3 μm in diameter. For comparison, Fig. 27(a) is of polystyrene exposed to about the same level of irradiation. Note that in the case of polystyrene no noticeable changes in surface quality are apparent.

PVA and CMC (CMC in particular) often showed development of surface cracks at damage levels in excess of 500 Mrads. During the SEM exposures, we were able to watch these cracks elongate, split, and widen on the video screen.

PAN and CH coating both behaved in a fashion similar to polystyrene in that no surface deterioration was visible even for doses as high as 3000 to 13 000 Mrad. Thus, from the viewpoint of surface quality, these shell materials seem to be quite durable against radiation damage.

The results from the polystyrene irradiation tests agree well with what has been previously published; polystyrene is stable up to 10^3 to 10^4 Mrad (Fig. 23). Similarly, the deterioration of CMC occurs at about the same irradiation level as reported for other cellulosics (Fig. 23, Table 3), i.e., about 10 Mrad.

Our results for PVA indicate that it is probably not an acceptable shell material for DT fills. It can withstand maximum damage levels of only ~10 Mrad. Unfortunately, because the hydrogen permeability of PVA is quite good, unacceptable radiation damage would occur in less time than it takes to diffusion-fill the shell (for our current shell sizes).

The results for PAN and CH are quite encouraging. PAN has a lower hydrogen permeability than polystyrene so it may make a better shell candidate. Likewise, the apparent stability of CH to radiation suggests that diffusion fill of DT through the ablator may be quite acceptable.

The observed stability of CH was perhaps the most surprising. It has been suggested that CH contains a number of unsaturated bonds. These are generally more easily damaged than saturated ones. Therefore, one might expect CH to be less damage-resistant than polyethylene or polypropylene (see Fig. 23). This is obviously not the case.

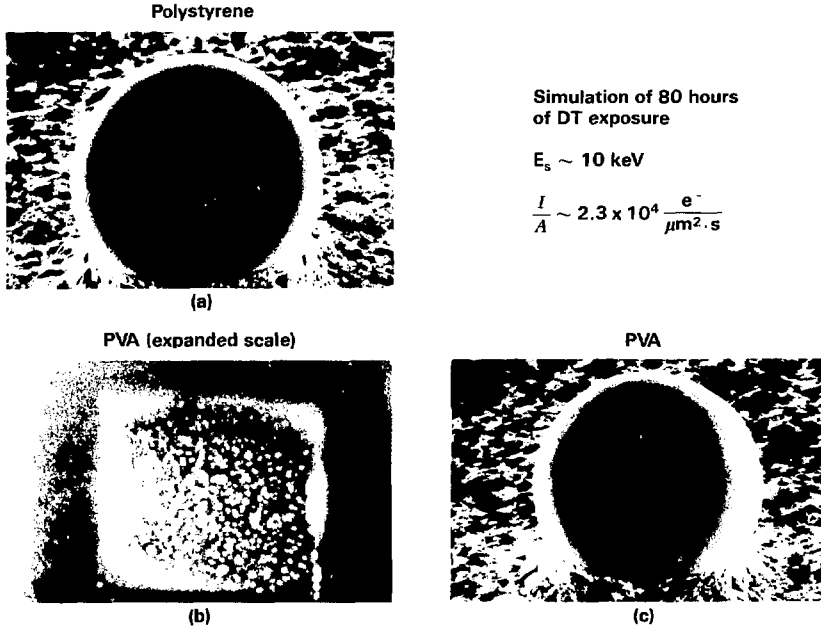

Figure 27. SEM photos showing: (a) polystyrene, and (b) and (c) polyvinyl alcohol both exposed to ~3000 Mrad of irradiation. The square "patch" in (b) shows the actual irradiated area on PVA; (c) is a view of the same area at lower magnification. Note, the area that was irradiated on polystyrene is not detectable. The spheres are about 180 μm in diameter.

It is possible that CH is more aromatic (like polystyrene) than has been previously thought. (Unfortunately, C^{13} NMR studies of CH were unable to quantify the fraction of aromatic, unsaturated, and aliphatic bonds in this polymer.)

One other possibility for the apparent resistance of PAN and CH is that they do undergo severe damage but that it is not observed as a surface deterioration. In particular, considerable cross linking and evolution of gas could occur and still not be evident as surface deterioration. Furthermore, in the actual use of DT, some reaction of DT either at the surface or *within* the polymer (DT solubility is quite high in many polymers) may lead to unacceptable damage.

One final question in relation to this study is the effect of high dose rates. As was mentioned in the introduction, the high dose rate may exacerbate the level of damage. This has no effect on the results from PAN, CH, or PS but may mean CMC and PVA could take higher doses without deterioration. It appears highly unlikely, however, that this effect would be enough to significantly change the results of these tests.

It is clear that the question of radiation damage to polymer shells and coatings cannot be adequately answered until actual DT tests are completed. Such tests are in progress here and at KMSF. This present study was designed only to give us preliminary indications of the damage resistance of several polymer shell candidates and identify possible early target design options.

Hydrostatic Tests of PVA Microsphere Strength

One of the most important properties of a microsphere is its strength. The microsphere must have sufficient strength to: (1) hold the required

gas fill and (2) withstand a large hydrostatic pressure during the fill procedure. We address here the problem of PVA strength as it relates to the gas-fill procedure, particularly gas-fill rates.

In brief, our results show that under low relative-humidity conditions, some of the uncoated 200 × 1 μm (nominal) PVA spheres can withstand hydrostatic pressures greater than 150 psi. Further experiments on coated spheres show that by applying a high-permeability coating (such as CH) on low-permeability shells such as PVA, much greater fill rates are possible because the strength added by the CH layer permits greater gas-pressure gradients during fill. The maximum permissible pressure gradient is probably dependent on the adhesive strength of the PVA to the CH layer. In the next few paragraphs, the results from these and other experiments are discussed in detail.

Effect of Pressure on Gas Fill Rates – Background

In general, three parameters limit the rate with which diagnostic or fuel gases can be added to microspheres: (1) the material permeability, (2) the shell dimensions (thickness and area), and (3) the pressure gradient across the wall. These parameters are related via a simple permeability expression easily derived from Fick's Law:

$$\dot{m} = \frac{AK_p\Delta P}{t_w} = \frac{\pi d^2 K_p \Delta P}{t_w} \quad , \tag{19}$$

where $\dot{m}$ is the mass rate (mol/s), A the area (m^2), K_p the permeability ($mol \cdot m/m^2 \cdot Pa \cdot s$), ΔP the pressure gradient (Pa), and t_w the shell wall thickness (m).

In the case of glass microspheres, reasonable fill rates are achieved by elevating the temperature to the point where the permeability becomes sufficiently large (~400°C). Furthermore, the elastic moduli and compressive strength of glass change very little over this temperature range, so that a large pressure gradient can still be maintained across the shell wall.

Filling plastic microspheres is not as easy. Although the permeability increases with temperature, this is often offset by a corresponding decrease in material strength thus reducing the allowable pressure gradient during fill.

Strength of PVA Shells Under a Hydrostatic Load

Failure of thin-walled spheres subjected to an external hydrostatic load is caused by either elastic buckling or by compression failure.[34] The buckling pressure (P_b) can be calculated from

$$P_b = \frac{8E}{3(1-\nu^2)^{1/2}}\left(\frac{t_w}{d}\right)^2 \quad , \tag{20}$$

where E is Young's modulus (psi), ν Poissons' ratio, and d the sphere diameter (m). Similarly the pressure for compressive failure (P_c) is given by

$$P_c = 4\sigma_c\left(\frac{t_w}{d}\right) \quad , \tag{21}$$

where σ_c is the compressive strength (psi). Thus, P_b and P_c represent the maximum permissible pressure gradients that may be applied to the shell during the fill cycle. If Eqs. (20) and (21) are substituted for the driving pressure (ΔP) in Eq. (19), two simple expressions are obtained that describe the *maximum* fill rate possible (just at the point of shell failure), that is

$$\dot{m}_{max} = \frac{8\pi K E\, t_w}{3(1-\nu^2)^{1/2}} \quad ; \quad (d = \text{constant}) \quad , \tag{22}$$

for conditions where elastic buckling dominates and

$$\dot{m}_{max} = 4\pi d K \sigma_c \quad ; \quad (t_w = \text{constant}) \quad , \tag{23}$$

where compressive strength is limiting.

Two interesting points emerge. First, in the elastic buckling region the maximum possible fill rate increases with wall thickness. Second, in the compression failure region, the maximum possible fill rate increases with the shell diameter.

Hydrostatic Pressure Testing System

The experimental system used to observe sphere failure under hydrostatic compression is shown schematically in Fig. 28. The spheres to be tested are mounted to a glass microscope cover using double-sided sticky tape. The sample is then placed in the pressure vessel (pressure tested up to 750 psi) and aligned with the two optical windows located at the ends of the cell.

High-pressure gas is fed to the cell through a regulator connected directly to a gas bottle. Pressure measurements are accurate to within ~ ±5 psi.

The sample is illuminated using a white light source and imaged onto a television screen. Thus, the failure of the spheres can be observed directly during the pressurization tests.

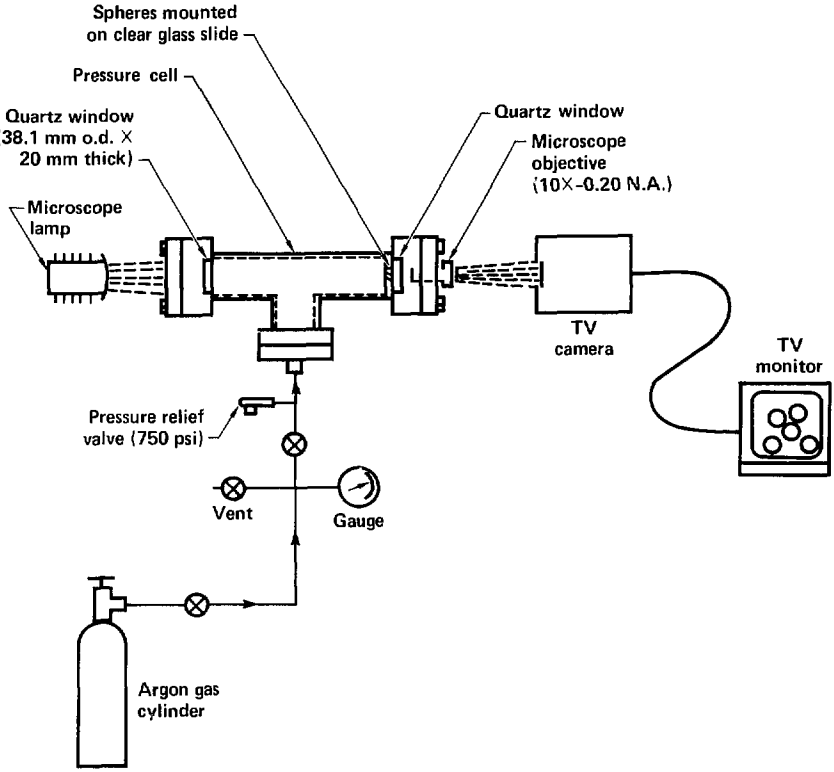

Figure 28. Schematic diagram of apparatus used for pressure tests on polymer microspheres.

Source and Relevant Properties of Polymer Microspheres Used in Strength Tests

The PVA microspheres were prepared from solution using the droplet-drying technique described previously. The spheres were nominally 180 to 200 μm in diameter and $\sim$1.5 μm in wall thickness.

Failure pressures for the PVA microspheres have been calculated using Eqs. (20) and (21) and the strength data in Table 2. These values are plotted in Fig. 29 as a function of shell aspect ratio.

Note that the buckling pressure curve (solid line, Fig. 29) is plotted for two different Young's modulus values, i.e., 0.5×10^6 and 1.1×10^6 psi. This is because Young's modulus for PVA is strongly dependent on relative humidity (Fig. 30); the values we used represent a reasonable range that might be expected based on the humidity at the time of our experiment.

Some of the PVA spheres tested were overcoated with CH that varied in thickness from about 7 to 22 μm and were prepared by Letts and Corley[35] using a plasma polymerization technique. The gas feed to the coating was hydrogen and trans-2-butene.

Results of Pressure Tests

The results of the microsphere pressure tests are summarized in Table 8. The data for uncoated

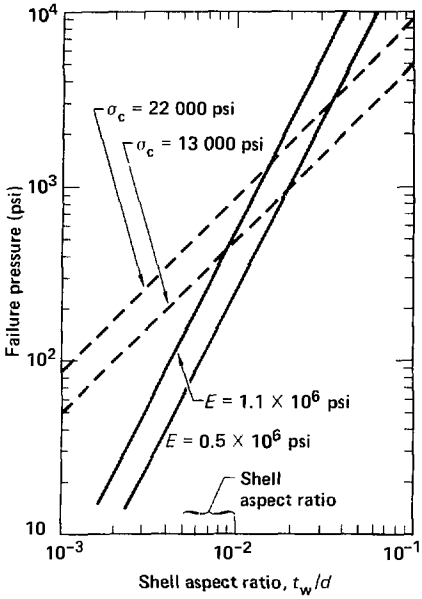

Figure 29. Calculated failure pressure vs aspect ratio for PVA microspheres. The solid lines are for buckling failure whereas the dashed lines represent compressive failure. The aspect ratios for the shells discussed in this report range from ~0.5 to 1.0 × 10 ^{2}.

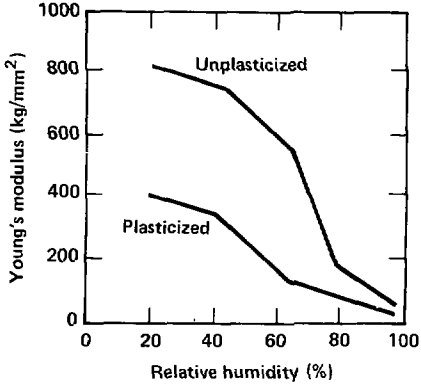

Figure 30. Young's modulus vs relative humidity (at 20°C) for unplasticized and plasticized polyvinyl alcohol film. The data are from Ref. 9.

PVA indicate failure by buckling only. This agrees well with the expected results based on Fig. 29. Note that for aspect ratios (t_w/d) less than ~0.02, buckling is the predicted failure mode. Typical examples of buckled PVA spheres are shown in Fig. 31. These are video-display photographs, before and after buckling, for the JP-87-G sample that failed in the 50 to 60 psi pressure region (see Table 8). (The circles at the centers of both the

Table 8. Summary of pressure test results.

Material	Batch number	Coating thickness (μm)	Microsphere dimensions: Wall thickness (μm)	Microsphere dimensions: Inside diameter (μm)	t_w/d (10^{-3})	Obs. failure mode	Failure pressure: Range (psi)	Failure pressure: Average (psi)
PVA	JP-69-E	0	1-2	180-220	5-9	Buckling	80-86	83
	JP-52	0	1-2	180	6-9	None	>147	>147
	JP-73-E	0	1-2	170-210	5-12	Buckling	100-145[a]	~120
	JP-87-G[b]	0	1-2	180-190	5-9	Buckling	50-60	57
	JP-78-E	0	1-2	210-220	5-10	Buckling	70-100	85
PVA/CH	HRA PVA 4	7.3	1-2	180	49	Compressive	740[c]	–
	HRA PVA 12	10	1-2	180-200	60	None	>740	>740
	HRA PVA 6	22	1-2	180-200	120	None	>740	>740
	HRA PVA 13	40	1-2	180-200	220	None	>740	>740

[a] One sphere did not collapse at maximum pressure (145 psi).

[b] Strength affected by high humidity.

[c] Only one out of four spheres failed.

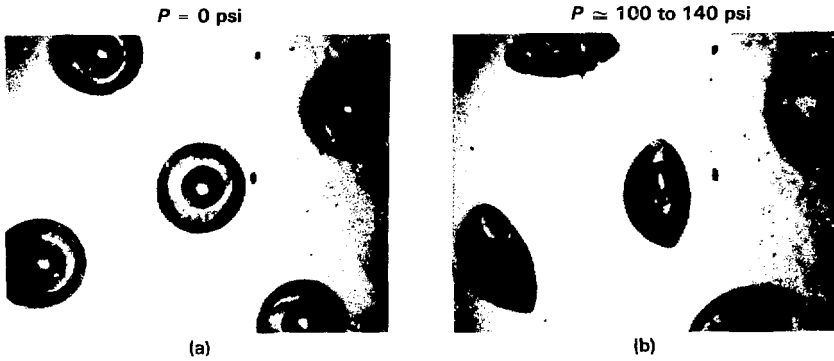

Figure 31. Photographs of video image of nominal 200 × 1–2 μm PVA spheres (a) before and (b) after buckling failure. (The circular spot at the center of the sphere is the contact point of the sphere on the adhesive tape.)

uncollapsed and collapsed spheres are the contact points with the adhesive tape used to secure the samples.)

After the pressure was released, the failed samples were re-examined to see if they had "re-inflated." Of all the samples tested, only one of the collapsed spheres was found to have returned to near its original shape. However, some defects from the buckling were still visible on the sphere surface.

The measured PVA buckling pressures (from ~50 to >145 psi) fall within the range expected for a Young's modulus between ~0.5 to 1.0 × 10^6 psi, a range that is quite reasonable for PVA considering the material's sensitivity to humidity (Fig. 30).

The method used to prepare the PVA spheres (i.e., droplet column) produced a range of residence times for the microspheres within the heated column. Consequently, the microspheres also experienced varying degrees of heat treatment. It is well known that the strength of PVA increases with heat treatment. Heating PVA causes a slight yellow discoloration—this color originates from associated small quantities of decomposition products. Thus a *qualitative* measure of the degree of heat treatment is the amount of yellow discoloration.

To evaluate whether heat treatment increases the strength, a set of PVA microspheres of about the same size but varying in color from clear to dark yellow were pressure-tested. The results are summarized in Table 9. These data clearly indicated the strength improvement possible with slight heating.

Overcoating PVA with CH dramatically increases the hydrostatic load needed to produce failure (Table 8). All but one of the CH-coated PVA spheres we tested held a minimum of 740 psi (the limit of our equipment). Figure 32 shows an SEM photograph of the PVA sphere with a 7.3-μm-thick coating that failed at ~740 psi. (In this particular experiment, we tested four spheres each coated with the same CH thickness. Only one of the four failed. It is not clear whether a coating or PVA shell defect may have led to the failure.)

It is probable that, with such high aspect ratios (i.e., t_w/d = 0.06 to 0.2), the failure mode for these coated samples is compressive failure. This assumes a low CH permeability for the pressurizing gas. With this assumption and using the results in Table 8, it is possible to estimate a lower

Table 9. Effects of heat treatment (as indicated by yellow coloration) on the buckling pressure of PVA microspheres (nominal 200 μm diam × 1 to 2 μm wall thickness from Batch JP-73-E).

Sphere number	Sphere color	Buckling pressure (psi)
1	Clear	64 to 103
2	Light yellow	105 to 117
3	Dark yellow	>145

$P_c \sim 740$ psi

Figure 32. SEM photograph of CH-coated PVA sphere that has undergone compressive failure at 740 psi.

limit for the compressive strength of CH of about 3500 psi. Until further data becomes available, this value may provide a useful benchmark for certain design calculations.

The large hydrostatic loads possible with a thick CH layer have important implications for filling low permeability PVA shells. Because CH has a very high permeability, it offers little diffusion resistance thus allowing the fill gases to rapidly permeate to the inner fuel capsule. Consequently, the greatest pressure gradient is across the inner container wall. Thus the limit to the pressure that can be applied to the coated sphere may well depend on the adhesive strength of the PVA to CH rather than the compressive strength of the CH.

Gas Permeability

A sizeable body of information exists on polymer permeabilities because of their widespread use in gas-barrier applications. Several excellent compilations of permeability data are given in Refs. 36 to 39; portions of the PVA data are summarized in Table 10.

One of the major reasons for selecting PVA as a microsphere material is its low hydrogen permeability. In Fig. 33 the hydrogen permeability of PVA is compared to values reported for a number of other polymers.

Doletsky et al.,[38] at KMSF have measured PVA permeability for deuterium and DT in PVA microspheres of differing polymer molecular weights. In general, the permeability decreases as the molecular weight of the polymer increases.

The permeability of PVA is strongly affected by humidity.[9] As shown in Table 10, small increases in humidity cause dramatic increases in

Table 10. Gas permeabilities (K_p) for PVA films. Conditions are assumed dry unless otherwise noted (RH = relative humidity).

Gas	T (°C)	K_p mol·m/m²·s·Pa	Ref. No.
H_2	25	3.1×10^{-18}	37
D_2	25	0.79 to 3.7×10^{-18} [a]	38
DT	25	0.97 to 2.1×10^{-18} [b]	38
He	20	3.3×10^{-19}	37
N_2	14	$<3.3 \times 10^{-19}$	37
N_2	14 (90% RH)	1.1×10^{-16}	37
O_2	25	3.0×10^{-18}	37
CO_2	23	3.3×10^{-19}	36
CO_2	23 (84% RH)	1.7×10^{-18}	36
CO_2	23 (94% RH)	4.0×10^{-15}	36
H_2S	25	2.3×10^{-16}	37
O_2	26	0.84×10^{-19}	9
O_2	35	1.3×10^{-19}	9
O_2	45	2.4×10^{-19}	9

[a] These values were measured for a range of PVA molecular weights (mol wt): (1) $K = 3.7 \times 10^{-18}$, mol wt = 14 000; (2) $K = 2.4 \times 10^{-18}$, mol wt = 115 000; (3) $K = 0.79 \times 10^{-18}$, mol wt = 330 000; and (4) $K = 1.3 \times 10^{-18}$, mol wt = 840 000.

[b] These values were measured for two PVA molecular weights, 115 000 and 330 000, respectively.

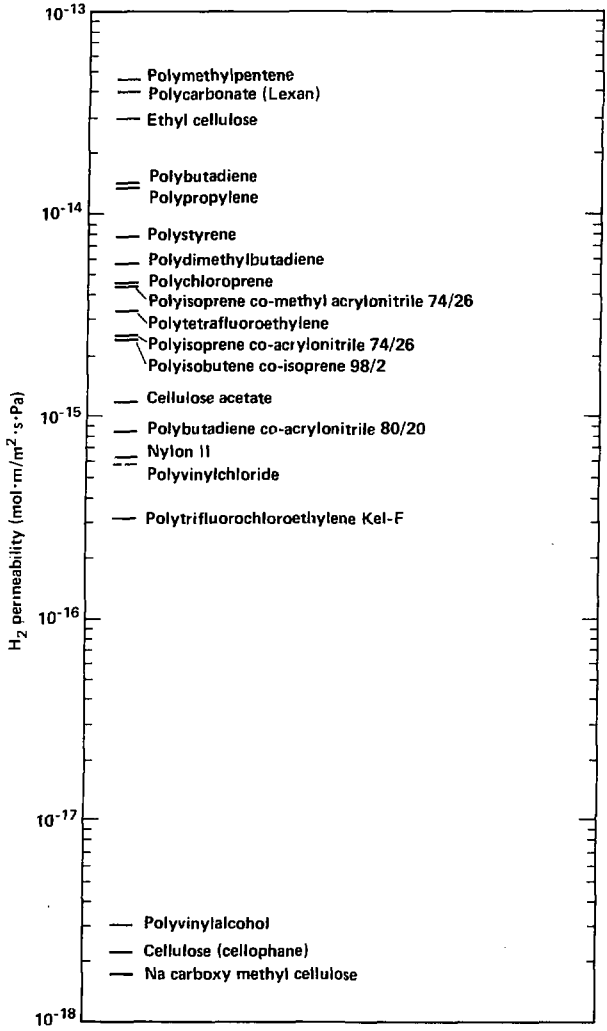

Figure 33. Hydrogen permeability data for a number of polymers at 25°C. Values are from Refs. 36 to 39. Note that the data reported for carboxymethylcellulose is for DT rather than H_2 (Ref. 38).

gas permeability. Thus, in many cases the range of reported permeabilities for a particular gas may be due to humidity effects. Not all polymers are as strongly affected by humidity changes as is PVA. For example, if the solubility of water in the polymer is small, then humidity generally has a smaller affect on permeability. On the other hand, if water is strongly absorbed by the polymer (as is the case for PVA), then it acts as a plasticizer, causing greatly increased permeability.[37]

Also note that the reported values for hydrogen agree well with those for both deuterium and DT. The slight difference could well be due to the difference in molecular weight of the gas and/or to variations in wall thickness of the microspheres (wall thickness reported to be 2.2 ± 0.5 μm). As with most polymers, the water permeability for PVA is much higher than that for other gases (Table 10). Water also behaves differently in that the permeability depends on the relative pressure drop across the polymer layer.[36]

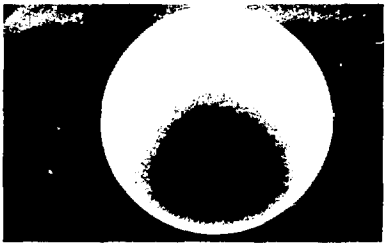

Figure 34. SEM photograph of a PVA microsphere coated via plasma polymerization with ~16 μm of CH coating. The coating work was carried out by Letts and Corley at LLNL.[40]

CH-Coated PVA Microspheres, Test Results

Approximately 15 batches of PVA microspheres were overcoated with a plasma-polymerized CH coating. This work was done by Letts and Corley[40] at LLNL and the details of the technique have been previously described.[7] The coating thickness varied from ~5 to 50 μm; a SEM photograph of a PVA microsphere coated with ~16 μm of CH is shown in Fig. 34.

Letts and Corley[40] addressed a number of different problem areas when coating polymer spheres that they had not encountered in previous work with glass. First, due to the relatively low thermal decomposition temperature of PVA (vs glass) the power to the plasma polymerization unit had to be lowered producing a corresponding decrease in the coating rate. In spite of this, Letts and Corley report excellent coating quality for thicknesses of up to ~50 μm and coating times of up to ~50 to 80 hours. Furthermore, they demonstrated that the spheres could be coated in several steps without adversely affecting the CH-coating quality.

Because the PVA spheres are so thin-walled (~1 to 2 μm), they are very light. This presented a second major coating problem in that many spheres bounced out of the coating container when standard agitation levels were used. By redesigning the coating container and by reducing the driving oscillator amplitudes the spheres could be successfully coated. Note that because of the increasing sphere density with coating thickness, it was found necessary to increase the vibration amplitudes as coating progressed.

One of the advantages of the CH coating process that we had not foreseen was the reduction in wall-thickness defects. Because the original PVA spheres were so thin, small variations in wall thickness made the spheres appear unacceptable when examined by the standard interference techniques.[41] However, once the CH ablator coating was added, the spheres easily met the required wall-uniformity specification discussed at the beginning of this report.

For further information on the coating studies the reader is referred to the work of Letts et al.[7,35,40]

Acknowledgments

The authors gratefully acknowledge the helpful discussions with Ray Downs and his research group at KMS Fusion on certain aspects of this work. The assistance of Paul McCarthy on the radiation damage studies and the helpful comments of Chuck Hendricks in regards to the dual-orifice generator are also appreciated.

References

1. J. H. Campbell, J. Grens, and J. Poco, "Preparation and Properties of Hollow Glass Microspheres for Use in Laser Fusion Experiments," Lawrence Livermore National Laboratory, Livermore, Calif., UCRL-53516 (1984).
2. R. L. Nolen, R. L. Downs, W. J. Miller, M. A. Elmer, N. E. Doletsky, and D. E. Solomon, "Fabrication of Glass Shells," Paper TuE1-1 in the Technical Digest on the Topical Meeting on Inertial Confinement Fusion, Feb. 7–9, 1978, San Diego, CA., Digest No. 78 CH1310-2EA, sponsored by the Optical Society of America.
3. L. B. Kool, R. L. Nolen, and K. W. Sherwood, *J. Vac. Sci. Technol.* **18**, 1233 (1981).
4. H. Shiraga, T. Mochizuki, S. Sakabe, K. Okada, A. Kikuchi, and C. Yamanaka, "Lateral Ablation-Pressure Distribution in a 1.053-μm-Laser-Irradiated Pellet," *Phys. Rev. Lett.* **1244(49)** 1982.
5. J. D. Kilkenny, B. J. MacGowan, and P. T. Rumsby, "Laser Driven Compression Experiments Using Low X-Ray Opacity Polymer Shells," *Appl. Phys. Lett.* **43**, 234 (1983).
6. V. S. Bushev, V. M. Dorogotoutsev, A. I. Isakov, N. S. Kobets, N. M. Kozyreva, V. V. Korshak, L. A. Krupinina, Yu. A. Merkul'ev, and A. I. Nikitenko, Trudy Ordena Lenia Fizicheskogo Instituta im. R. V. Lebedava, **12** (1980), pp. 72–83. Translation available from Lawrence Livermore National Laboratory, Livermore, Calif., UCRL-TRANS-11924 (1983).
7. S. A. Letts, D. W. Meyer, and L. A. Witt, "Ultrasmooth Plasma Polymerized Coating for Laser Fusion Targets," *J. Vac. Sci. Technol.* **19**(3) 739, Sept./Oct. (1981).
8. R. Crawley, KMS Fusion, Inc., Ann Arbor, Mich., private communication (December 1982).
9. *Encyclopedia of Polymers*, vol. 14, p. 149, "Vinyl Alcohol Polymers."
10. M. Goldfin, J. Yerushalmi, R. Pfeffer, and R. Stinnar, "Break-up of Linear Capillary Jet of a Viscoelastic Fluid," *J. Fluid Mech.* **38**, 44 (1969).
11. C. D. Hendricks and J. L. Dressler, "Production of Glass Balloons for Laser Targets," *Bull. Amer. Phy. Soc. Series II* **21**, 1137 (1976).
12. J. M. Schneider and C. D. Hendricks, "Source of Uniform-Sized Liquid Droplets," *Rev. Sci. Inst.* **35**, 1349 (1964).
13. C. D. Hendricks and S. Babil, *J. of Physics E* **5**, 905 (1972).
14. R. J. Calliger, R. J. Turnbull, and C. D. Hendricks, *Rev. Sci. Instrum.* **48**, 846 (1977).
15. J. W. S. Rayleigh, *Proc. London Mathematical Soc.*, vol. IV, p. 4 (1878).
16. D. H. Charlesworth and W. R. Marshall, Jr., "Evaporation from Drops Containing Dissolved Solids," *A.I.Ch.E. Journal* **6**, 9 (1960).
17. J. A. Duffie and W. R. Marshall, Jr., "Factors Influencing the Properties of Spray Dried Materials," *Chem. Eng. Progress, Part I* **49**, 417 (1953); *Part II* **49**, 480 (1953).
18. W. E. Ranz and W. R. Marshall, Jr., "Evaporation from Drops," *Chem. Eng. Progress* **48**, 173 (1952).
19. E. J. Crosby and W. R. Marshall, Jr., "Effects of Drying Conditions on the Properties of Spray-Dried Particles," *Chem. Eng. Progress* **54**, 56 (1958).
20. W. R. Marshall, Jr., "Heat and Mass Transfer in Spray Drying," *Trans. Amer. Soc. Mech. Eng.* **77**, 1377 (1955).
21. D. R. Dickinson and W. R. Marshall, *A.I.Ch.E. Journal* **14**, 541 (1960).
22. K. Masters, *Spray Drying* (CRC Press, Cleveland, Ohio, 1972), Chapter 8.
23. D. W. Van Krevelen, *Properties of Polymers, Their Estimation and Correlation with Chemical Structure* (Elsevier Scientific Publishing Co., New York, N. Y., 1976).
24. O. Griffin Lewis, *Physical Constants of Linear Homopolymers* (Springer–Verlag, New York, N. Y., 1968), pp. 158–159.

25. "Properties and Applications of Poly (vinyl alcohol)," *Soc. of Chem. Ind. London*, Monograph No. 30, London, England (1968).
26. J. G. Pritchard, "Poly(vinylalcohol), Basic Properties and Uses" (Gordon and Breach, Inc. New York, N. Y., 1970).
27. D. C. Phillips, "The Effects of Radiation on Electrical Insulators in Fusion Reactors," AERE-R8923, AERE, Harwell, England (1978).
28. A. Charlesby, *Atomic Radiation in Polymers* (Pergamon Press, Elmsford, N. Y., 1960).
29. R. O. Bolt and J. G. Carroll, *Radiation Effects in Organic Materials* (Academic Press, New York, N. Y., 1963).
30. W. W. Parkinson and O. Sisman, "The Use of Plastics and Elastomers in Nuclear Radiation," *Nuclear Engineering and Design* **17**, 247 (1971).
31. W. E. Skiens, "Sterilizing Radiation Effects on Selected Polymers," *Radiation Phys. Chem.* **15**, 47 (1980).
32. M. H. Van de Voorde, "Effects of Radiation on Materials and Components," CERN 70-5 (1970).
33. J. F. Kirchen and R. E. Bowman, *Effects of Radiation on Materials and Components* (Rheinhold Publishing Corp., 1964).
34. R. L. Woerner, B. W. Weinstein, I. M. Moen, and J. C. Rittmann, *Working Strengths and DT Fill Procedures for Glass Microsphere Laser Fusion Targets*, Lawrence Livermore National Laboratory, Livermore, Calif., UCRL-82728 (1979).
35. S. Letts and R. Corley; Lawrence Livermore National Laboratory, personal communication (1983).
36. J. Crank and G. S. Park, *Diffusion in Polymers* (Academic Press, 1968).
37. J. Brandrup and E. H. Immergect, Eds., *Polymer Handbook*, 2nd ed., pp. 229–240.
38. N. E. Doletsky, M. A. Ebner, L. B. Kool, P. J. Lennon, R. L. Nolan, Jr., J. J. Rolen, and D. E. Solomon, "Polymer Research," *1977 Annual Report on Laser Fusion Research*, KMS Fusion, Inc., Ann Arbor, Mich., pp. 1-25 to 1-33.
39. D. W. Van Krevelen, op cit., pp. 403–424.
40. S. Letts and R. Corley; Lawrence Livermore National Laboratory, report in preparation (1984).
41. B. W. Weinstein and C. D. Hendricks, *Interferometric Measurement of Laser Fusion Targets*, Lawrence Livermore National Laboratory, Livermore Calif., UCRL-78477 (1977).

LR:js